Author/s:
Zahtila, T;Lam, WK;Chan, L;Sutherland, D;Moinuddin, K;Dai, A;Skvortsov, A;Manasseh, R;Ooi, A

Title:
On the propagation of planar gravity currents into a stratified ambient

Date:
2024-03

Citation:
Zahtila, T., Lam, W. K., Chan, L., Sutherland, D., Moinuddin, K., Dai, A., Skvortsov, A., Manasseh, R. & Ooi, A. (2024). On the propagation of planar gravity currents into a stratified ambient. Physics of Fluids, 36 (3), https://doi.org/10.1063/5.0190835.

Persistent Link:
https://hdl.handle.net/11343/355999

RESEARCH ARTICLE | MARCH 04 2024

On the propagation of planar gravity currents into a stratified ambient

Tony Zahtila ; Wai Kit Lam ; Leon Chan ; Duncan Sutherland ; Khalid Moinuddin ; Albert Dai ; Alex Skvortsov ; Richard Manasseh ; Andrew Ooi

Physics of Fluids 36, 036601 (2024)
https://doi.org/10.1063/5.0190835

Physics of Fluids ARTICLE pubs.aip.org/aip/pof

On the propagation of planar gravity currents into a stratified ambient

Cite as: Phys. Fluids **36**, 036601 (2024); doi: 10.1063/5.0190835
Submitted: 8 December 2023 · Accepted: 6 February 2024 ·
Published Online: 4 March 2024

Tony Zahtila,[1] Wai Kit Lam,[1] Leon Chan,[1] Duncan Sutherland,[2] Khalid Moinuddin,[3] Albert Dai,[4] Alex Skvortsov,[5] Richard Manasseh,[6] and Andrew Ooi[1]

AFFILIATIONS

[1]Department of Mechanical Engineering, University of Melbourne, Parkville, VIC 3010, Australia
[2]School of Science, University of New South Wales, Canberra, ACT 2600, Australia
[3]Institute of Sustainable Industries and Liveable Cities, Victoria University, Werribee, VIC 3030, Australia
[4]Department of Engineering Science and Ocean Engineering, National Taiwan University, Taipei 10617, Taiwan
[5]Maritime Division, Defence Science and Technology Group, Fisherman's Bend, VIC 3207, Australia
[6]Department of Mechanical and Product Design Engineering, Swinburne University of Technology, Hawthorn, VIC 3122, Australia

[a)]Author to whom correspondence should be addressed: tzahtila@stanford.edu

ABSTRACT

Gravity currents are of high interest both for their relevance in natural scenarios and because varying horizontal buoyancy presents a canonical problem in fluid mechanics [Huppert, "Gravity currents: A personal perspective," J. Fluid Mech. **554**, 299–322 (2006)]. In this paper, attention is directed to gravity currents with a full-depth lock release propagating into a linearly stratified ambient fluid. For the case of an unstratified ambient, similarity solutions are known to capture the evolving height profile of the gravity current. We will compare this solution class with numerical data from high fidelity simulations. The presence of ambient stratification (quantified by the stratification intensity, S) introduces internal gravity waves that interact with the propagating current head, which will inhibit Kelvin–Helmholtz billows, decelerate current propagation, and smooth the shape of the current head. We perform direct numerical simulations of planar two- and three-dimensional gravity currents released into stratified ambient fluid of varying S and analyze the gravity current kinematics. Our analysis complements existing findings from performed laboratory and numerical experiments [Dai *et al.*, "Gravity currents propagating at the base of a linearly stratified ambient," Phys. Fluids **33**, 066601 (2021)] that show a stratified ambient modifies the current front velocity. Previous literature employed has inconsistent Reynolds numbers and boundary conditions, complicating interpretations. In the present numerical campaign, a closer analysis clarifies influence of the top boundary condition choice on formation and structure of the internal gravity waves. While acknowledging there is no available choice for a high-accuracy simplified numerical representation of a free-surface, a family of profiles for internal wave formation emerges varying with buoyancy Reynolds number and top boundary condition selection. The subsequent results appraise similarity solutions for the distribution of the heavy fluid in the gravity current. Our results show that for unstratified and low stratification ambient fluid, height profiles permit a similarity solution but higher values of S are less amenable; these profiles suggest a continuing time dependency on the traveling internal wave.

I. INTRODUCTION

Gravity currents occur when a fluid of a given density propagates into an ambient fluid of a lower density.[1] Subject to a gravitational field, this density differential drives the flow, transporting fluid and passive scalars potentially very far from their origin. Gravity currents occur in many environmental scenarios, for example, smoke-laden gravity currents which originated from bushfires near Canberra, Australia in 2019, led to severe and unexpected smoke inundation of densely populated areas, over a period of weeks to months. It was also found that the measured particulate concentration was similar across cities hundreds of kilometers apart,[3] in accordance with the notably large scale of the 2019 Australian bushfires. In another example, light detection and ranging (LiDAR) measurements were used to report characteristics of a smoke filled gravity current originating from a bushfire in California, United States of America.[4] The current was recorded as approximately 2 km in height, traveling more than 25 km at speeds up to 16.2 km/h.

In the laboratory setting, gravity currents are typically modeled as a lock exchange problem, featuring a tank with a barrier separating regions of heavier and lighter fluid. When the barrier is removed, the heavier fluid forms a gravity current and transports horizontally into the region of lighter fluid (termed the ambient fluid). This flow has been extensively studied experimentally[5–9] and numerically.[10–13] A feature reported in all studies above is the presence of Kelvin–Helmholtz billows at the top of the gravity current. These billows are the main mechanism responsible for the mixing of fluid inside the gravity current with the ambient fluid. Another common finding is that gravity current propagation enters various phases. Initially, an *acceleration* phase commences whereby the heavy fluid accelerates from rest and the head of the current is formed. Afterward, the gravity current goes through three different phases, the *slumping*, *inertial*, and *viscous* phases. During the *slumping* phase, the front location has been reported[14] to follow an approximately $t^{1.0}$ power law and hence the front velocity of the current is constant. Additionally, a bore is formed during the slumping phase and the bore is reflected off the left most boundary of the tank or the computational domain, which arises because the left side of the tank initially contains heavier fluid. The *slumping* phase velocity is constant until the bore catches up with the front of the current. The dynamics of the bore and its interaction with the gravity current head has been detailed.[6,13] The formation of the bore is a consequence of the current head's forward propagation at early intervals. For a propagating current, by considering a reference frame moving with the current head, it was observed that the ambient fluid is advected backward above the current in response to the current's propagation.[15] That finding was established in the context of a lock-exchange flow propagating on a 2% slope.

Once the bore catches and dilutes the gravity current head, the current transitions into the *inertial* phase and the velocity of the current head starts to decelerate. Experimental and numerical data,[2,9,12,15,16] which are compared in Table I, have shown that the exponent of the power law for the front location of the current decreases to 2/3, i.e., an approximately $t^{2/3}$ power law is present during the *inertial* phase. This decay agrees with similarity solutions of the shallow water equations.[17] In the *inertial* phase, the movement of the current is believed to occur mainly under the balance of buoyancy and inertial forces. After the *inertial* phase, viscous forces dominate over inertial forces and the current movement is mainly attributable to the balance of viscous and buoyancy forces.

Cantero *et al.*[12] investigated the front velocity of the gravity current and also focused on the increasing prominence of the three-dimensional (3D) effects emerging with higher Reynolds number. By contrasting the output of two-dimensional (2D) and 3D simulations, it was noted that enhanced vortex coherence of 2D simulations heightened vortex interactions resulting in spurious front velocities in the inertia phase. Additionally, in both lock-exchange experiments and 2D simulations,[18] it was reported that slumping velocity was independent of the aspect ratio (AR) of the volume of heavy fluid for ratio of streamwise length (l_0) to depth of release (h_0), for $AR = l_0/h_0 = 2 - 8$.

A great deal of numerical and experimental work has gone into developing models for gravity currents and understanding the variation in possible release types and ambient fluid composition. The studies mentioned so far have concentrated on situations where the ambient fluid is homogeneous. Situations where the gravity current moves into an ambient environment that is stratified have also received attention.[2,18,19] More complex cases where the gravity current moves into stratified ambient with submerged canopy has also been investigated.[20]

In this paper, we consider the situation where a planar 3D gravity current propagates into an ambient environment with a thermal inversion, i.e., where there is linear stable stratification with larger density at the bottom of the domain and smaller density at the top. In this scenario, the movement of the gravity current will generate internal gravity waves that interact with the Kelvin–Helmholtz billows atop the gravity current. This interaction governs the dynamics of the gravity current head for an important interval of time where a transition occurs. The main study presented in this paper is carried out using data from high fidelity 3D direct numerical simulations (DNSs) with different ambient stratification intensity (S). Pertinent insights will be given on the existence of similarity solutions and the use of data-driven decomposition to identify existence of a similarity regime.

First, however, we will run a larger set of 2D simulations which vary the Reynolds number and choice of top boundary condition, which constitutes varying computational simplifications of a free surface. We will aim to clarify the prevalent ambiguities of the no-slip top boundary condition yielding numerical datasets that better agree with experimental campaigns[2] which has not been yet addressed in previous work. In that reference, an inconsistent buoyancy Reynolds number featured between numerical ($Re_b = 5000$) and experimental ($Re_b = 20\,000$) datasets yielding agreement in the current front location profiles. Highly applicable to the present effort, justification for the top boundary condition employed in the numerical simulation was not adequately explained, which aims to emulate a free surface via the less intuitive choice of a no-slip boundary. That approach deviated from the better founded rigid-lid approximation which features a free-slip condition, and moreover, there is no consensus in the lock-exchange context on appropriate free-surface numerical representation. This is an important due-diligence investigation associated with

TABLE I. Previously conducted numerical and experimental campaigns into gravity currents which vary the parameters of interest, buoyancy Reynolds number Re_b, ratio of streamwise length to depth of release l_0/h_0, stratification intensity S, and simulation runtime interval $t_{max}U_b/h_0$.

Authors	DNS/LES/experiments	Re_b	l_0/h_0	S	$t_{max}U_b/h_0$
Pelmard *et al.*[15]	LES	1000–60 000	1.93	0.0	∼49
Cantero *et al.*[12]	DNS	895–8950	1–8.5	0.0	∼30
Marino *et al.*[9]	Experiments	2790-228 000	0.25–1	0.0	∼70
Dai *et al.*[2]	DNS	5000	1.33	0.1–0.98	∼60
Lam *et al.*[16]	DNS	3450–10 000	1	0.0–0.8	∼60

numerical datasets that requires attention because internal gravity waves influence internal bore movement inside the gravity current, which impacts the mixing of fluid at the head of the gravity current. Further details of how the mixing of fluid changes the decay rate of the gravity current head velocity during the slumping and inertia phases will be investigated.

The spreading of a gravity current has piqued the interest of many researchers for the apparent geometric self-similarity that can be observed.[21,22] Similarity solutions arise when appropriate scaling exists to relate the problem's independent and dependent variables.[23] For the present class of lock-exchange problems, the *inertial* and *viscous* propagation phases feature a simple balance of inertial-buoyancy and viscous-buoyancy forces and an equation may be derived for the front position evolution.

In this paper, scaling for two models are evaluated, the first is the simple box model which boldly assumes that the gravity current retains a box shape[24] contrasted with similarity solutions to the shallow water equations[25] which incorporate the distinctive current front "nose" profile. In addition to appraising the validity of similarity solutions by scaling the generated datasets, we also add data-driven determination of whether the presence of a self-similar profile is to be expected. This is achieved by computing the singular value decomposition (SVD) of the scaled profiles and thereafter analyzing the steadiness of modal contributions to the current depth profiles.

II. PROBLEM FORMULATION

A. Governing equations and computational setup

In this study, data are obtained by solving the incompressible Navier–Stokes equations. The Boussinesq approximation is utilized to approximate buoyancy effects, which neglects the effects of density differences except for in the buoyancy term,[26] and this methodology has been widely adopted in the reference numerical databases mentioned throughout this paper. We are interested in the case where the heavy fluid with a density ρ_C propagates into an ambient density field that is linearly stratified with the value of density ρ_0 at the top of the domain and ρ_B at the bottom of the domain. Utilizing the density field to visualize the gravity current is difficult when stratification is present because there is no straightforward method to differentiate between fluid parcels entrained by the gravity current and ambient fluid.

As a remedy, in order to provide a more accurate representation of the propagating gravity current, we will solve an additional equation to track evolution of a passive scalar, C. The passive scalar is assumed to be a substance that is advected by the fluid without changing the properties of the fluid flow (smoke, dust, moisture particles, molecules of pollutant). The governing equations are numerically solved here to simulate gravity currents propagating into a stratified ambient fluid (which have been employed previously for this specific flow physics[2]),

$$\frac{\partial \tilde{u}_i}{\partial \tilde{x}_i} = 0, \tag{1}$$

$$\frac{\partial \tilde{u}_i}{\partial \tilde{t}} + \tilde{u}_j \frac{\partial \tilde{u}_i}{\partial \tilde{x}_j} = -\frac{\partial \tilde{p}}{\partial \tilde{x}_i} + \frac{1}{Re_b} \frac{\partial^2 \tilde{u}_i}{\partial \tilde{x}_j \partial \tilde{x}_j} + \tilde{\rho} e_i^g, \tag{2}$$

$$\frac{\partial \tilde{\rho}}{\partial \tilde{t}} + \tilde{u}_j \frac{\partial \tilde{\rho}}{\partial \tilde{x}_j} = \frac{1}{ScRe_b} \frac{\partial^2 \tilde{\rho}}{\partial \tilde{x}_j \partial \tilde{x}_j}, \tag{3}$$

$$\frac{\partial C}{\partial \tilde{t}} + \tilde{u}_j \frac{\partial C}{\partial \tilde{x}_j} = \frac{1}{ScRe_b} \frac{\partial^2 C}{\partial \tilde{x}_j \partial \tilde{x}_j}, \tag{4}$$

where all variables with a tilde on top are dimensionless, u_i are the components of the velocity field, p the pressure, ρ is the density, e_i^g the unit vector in the direction of gravity, and C is the concentration of the passive scalar. The subscript $i = 1$ will correspond to the x-direction, and $i = 2$ and 3 will be associated with y and z, respectively. The depth of release h_0 is taken to be the length scale and the buoyancy velocity, $U_b = \sqrt{g' h_0}$ is the employed velocity scale with $g' = g(\rho_C - \rho_0)/\rho_0$ the reduced gravity. The timescale is simply h_0/U_b. The dimensionless density and pressure are defined as

$$\tilde{\rho} = \frac{\rho - \rho_0}{\rho_C - \rho_0} \quad \text{and} \quad \tilde{p} = \frac{p}{\rho_0 U_b^2}.$$

The two dimensionless parameters in Eqs. (1)–(4), the buoyancy Reynolds and Schmidt numbers, are defined as

$$Re_b = \frac{U_b h_0}{\nu} = \sqrt{\frac{g' h_0^3}{\nu^2}} \quad \text{and} \quad Sc = \frac{\nu}{\kappa},$$

where ν is the kinematic viscosity and κ is the diffusion coefficient for both the density and passive scalar field. Under this formulation, we assume that the heavy fluid and ambient fluid are fully miscible and have the same value of ν. Furthermore, the Schmidt number is set to unity, Sc = 1. However, it has been reported that gravity current dynamics are not sensitive to Sc provided that Sc $\approx O(1)$ or larger, especially at large Re_b.[27]

The equations of motion are solved using the spectral element code Nek5000[28] on the computing facilities at the University of Melbourne[29] and the National Computing Initiative (NCI) Australia. Throughout, data will be extensively compared with the complementing laboratory experimental setup.[2] It is worthwhile to report the reference laboratory settings for the full-depth release lock-exchange problem the present numerical study simulates. There, the heavy fluid (saline) is placed in a smaller chamber in the left side of the tank separated by a glass sheet from the right side of the tank, which is filled with stratified fluid. The initial streamwise length (l_0) and height (h_0) of the heavy fluid in the full-depth release of the heavy fluid are $h_0 = 9$ cm and $l_o = 12$ cm, and the width of the tank is $L_z = 20$ cm.

The computational schematic for the present numerical study (which mirrors the laboratory experimental setup) is shown in Fig. 1. The initial configuration of the heavy fluid is indicated by the red box. To mimic the experiments, the aspect ratio is set to $l_o/h_0 = 4/3$. The length, height, and width of the computational domain are denoted, respectively, as L_x, L_y, and L_z. Similar to the experiments, we will only consider the full depth lock-release problem where the initial height of the current extends to the top of the computational domain, i.e., $h_0 = L_y$. In the presentation of results, all the length scales are non-dimensionalized with h_0. Ideally, we would like L_x to be as large as possible to ensure that the right boundary is sufficiently far enough so as not to influence the flow generated by the gravity current. We have carried out our simulations using $L_x/h_0 = 25$, and an additional $L_x/h_0 = 37.5$ case was run to ascertain dependency of our results on L_x, and it was found that the $L_x/h_0 = 25$ domain sufficed to ensure reliable data. For the spanwise direction, we will use $L_z/h_0 = 1.5$, which is similar to values used by many preceding authors.[2,12]

The details of the utilized mesh for the spectral element method (SEM) numerical solver are provided in Table II. As a brief introductory remark on meshes for SEMs, the domain is first discretized into a

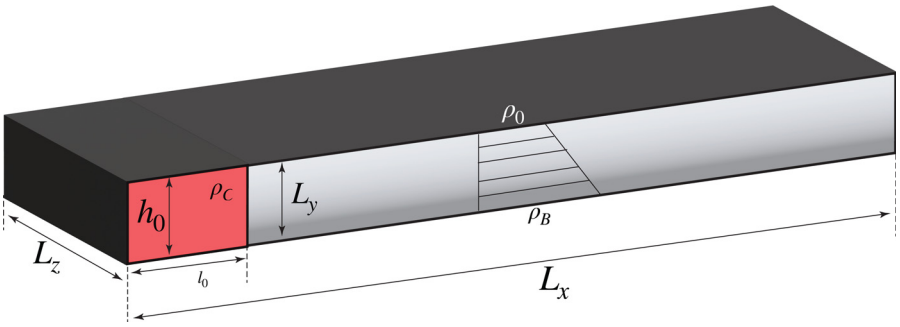

FIG. 1. Schematic of the planar full-depth lock-exchange release in a linearly stratified ambient fluid computational domain. Pertinent lock-release and computational parameters annotated.

TABLE II. Computational grids utilized in this study. The table specifies N_i the number of spectral macro elements used in each direction, N_p the polynomial order, and G_p, the number of unique grid points.

Case	N_x	N_y	N_z	N_t	N_p	G_p
Main	300	21	15	94 500	8	0.5×10^8
Hi-res	350	60	20	420 000	8	2.2×10^8
2D	500	30	…	15 000	8	0.9×10^6

number of "macro-elements," and inside each of these elements, points are distributed unevenly, in this case on a Gauss–Lobatto–Legendre (GLL) distribution and a high-order polynomial is fit to these points. Between macro-elements, only C_0 continuity is preserved. In this study, for all cases run, the polynomial order is set to $N_p = 8$. Spectral element solvers are highly accurate with low numerical dissipation and because only C_0 continuity exists between spectral elements, visualization of derivative terms that show smooth results is a common gauge for a well-resolved flow field.[30,31] It should further be noted that SEM solvers typically offer rapid convergence with mesh refinement for primitive variable statistics, which are continuous between elements in the solution procedure. Examples include time-averaged streamwise velocity in confined wakes[32] and mean wall-normal velocity profiles in wall-bounded origami surface simulations.[33] To validate the present simulations, we investigate two mesh resolutions. As a reference, the wall-normal spacing to local Kolmogorov scale ratio for both mesh resolutions is plotted in Fig. 2 after $tU_b/h_0 = 35$ time units for the unstratified case, $S = 0$. The unstratified case was chosen because it is associated with the highest observed propagating current front velocity u_F of the stratification intensities investigated. For spectral element simulations, systematic study of grid-convergence has revealed that the turbulence dynamics can be considered safely resolved when grid spacing in directions of high-dissipation $\Delta_{x_i}/\eta < 16$[34] but this may be overly stringent for finite computing budgets and many turbulence statistics are captured with less grid resolution. The time step size was adapted to maintain a Courant number restriction, $Co = u\Delta t/\Delta x < 0.5$.

A comparison of the dimensionless current front location generated from both mesh resolutions is presented in Fig. 2(c) and we observe excellent agreement. The streamwise grid requirement precedent[35,36] for gravity current simulations has been stated as $\Delta x \approx (ReSc)^{-1/2}$. Because we use a spectral element mesh, the intra-element spacing minimum Δx_{min} is finer than this requirement and the maximum Δx_{max} is greater. Additionally, a stretching function is applied in the wall-normal direction in order to fully resolve the current nose. Given data collected from the different resolution meshes yielded excellent agreement between the propagating current front location, which is a major quantity of interest in this paper; we therefore conclude that with our finite computing budgets, for the statistics we focus upon in this study, the "main" resolution from Table II suffices and will be employed for higher stratification intensities. It is worthwhile to point out that specific study of the small-scale motions would require use of the higher resolution mesh. Thus, some discussion of these requirements for accurate and fully resolved DNS is required. The wall-normal direction is chosen for investigation in Fig. 2 because (i) the aforementioned streamwise grid requirements have already been computed[35,36] and (ii) subsequent results in this manuscript show that there is only minimal variation between 2D simulations that neglect the spanwise direction and 3D simulations. It should be noted that when a measure in all directions was computed, $\Delta l/\eta$, where $\Delta l = \sqrt[3]{\Delta x \Delta y \Delta z}$ was computed, the mean value $\Delta l/\eta$ in the propagating current head was approximately 15.0 in the main simulation set and approximately 5.0 in the high-resolution case. Thus, whether or not this can be considered fully resolved DNS still requires analysis of the small-scale features that forms forthcoming work, but certainly is typical among DNS computations performed today.

B. Boundary conditions

This section discusses the finer details of computational representation of the laboratory lock-exchange experiment, which constitutes a variable density fluid confined in an open tank, i.e., a free surface exists. The primary variation in the computational setup of existing numerical contributions is in modeling of the free surface. This problem is inherited from the general difficulties in computational representation of free surfaces, where it is known that un-approximated time-dependent free surface boundaries which move and deform present stringent vertical-resolution requirements to be accurately captured.[37] More commonly, the free surface is simplified and approximated. This is an active area of numerics research, for example, in open channels.[38] The often favored computationally efficient approach is the rigid-lid simplification, which imposes a free-slip boundary condition for the surface-tangential stresses on a flat surface. Although it is the most common treatment of a free surface, comparison with surface-resolved large eddy simulation (LES) has revealed that instantaneous turbulent structures markedly differ by methodology adopted for the free surface representation.[39] This substantiates the generic finding that despite the popularity of the rigid-lid simplification, it may be severely limited for some flows.

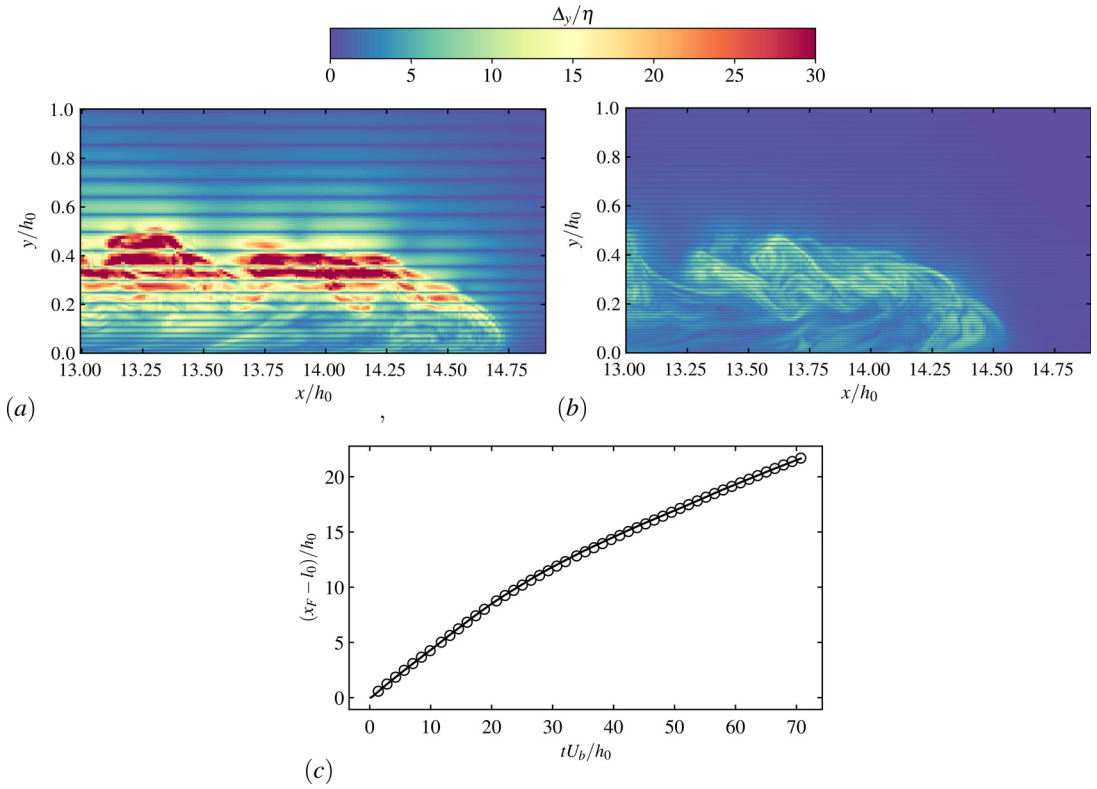

FIG. 2. Grid-spacing to instantaneous Kolmogorov scale, Δ_y/η comparison for 3D meshes used in this study: (a) main and (b) high-resolution. Spectral elements feature an uneven GLL distribution grid-spacing and so the local grid resolution varies with intra-element spacing. Dimensionless front location against time plotted in (c) with open circles corresponding to the high-resolution case and solid black line to the main mesh result.

Returning to the present gravity current context, standard rigid-lid boundary condition at the top boundary has been employed by several researchers.[15,20] Additionally, free-slip boundary conditions were used at the top and bottom boundaries to simulate intrusion currents.[40] In lieu of employing the rigid-lid approximation at the top boundary, the alternative choice of no-slip boundary condition has also featured prominently in unsteady gravity currents.[2,18,41] The basis for this alteration is the resultant agreement between generated numerical data and experiments. Therefore, further attention is warranted as the intuitively formulated approach to free surfaces has not hitherto been the preferred numerical treatment in preceding numerical lock-exchange simulations.

Some prior contributions have also sought to address this topic. When comparison of no-slip and free-slip top boundary condition was the explicit focus of numerical simulations performed, it was found that full-depth release heightened the role of top boundary condition, but only minimal difference in the front location propagation was observed.[42] As the ambient fluid was unstratified in that comparison, there is only a partial relevance of those findings to the present campaign. It can be postulated that comparing with experimental data, both no-slip and free-slip boundary conditions are plausible approximations of the tank free surface. Hence, discrepancy with experimental data should be attributable to the boundary condition used at $y = L_y$. This has been hinted at by previous researchers who compared and contrasted laboratory and numerical data[18] where correspondence was included which explicitly deduced that the nature of the boundary condition at the free surface is significant for some features of the flow. Accordingly, we observe results that are quite sensitive to the boundary condition used at $y = L_y$, especially for the larger values of stratification intensity S due to the emergent internal waves. It should be noted that examination of the boundary condition on the surface the gravity current is traveling on has also received attention[43,44] where mechanisms responsible for lobe-cleft instabilities were investigated, and more highly pertinent to the present effort, it has been found that a no-slip wall substantially reduces the front propagation of the current head compared with the free-slip boundary condition, and as a consequence, in the no-slip case, the Froude number is reduced.

It remains to complete the numerical details for the present setup. For all simulations carried out in this paper, free-slip boundary conditions are applied at the two ends of the streamwise domain, $x = 0$, and $x = L_x$ for the velocity, density and passive scalar fields. Periodic boundary conditions are used in the spanwise, z-direction. At the bottom, $y = 0$ boundary, a no-slip boundary condition is used for the velocity field, further, Neumann zero gradient boundary conditions are used for density and passive scalar fields. The choice of free-slip boundary conditions in the streamwise direction, and periodicity in the spanwise direction requires some brief remark to contextualize the expected effect of these choices. For the streamwise direction, choice of no-slip for the left and right tank walls would be more physically

TABLE III. Summary of cases run in the present study and numerical details. Note that 2D simulations vary the top boundary condition and buoyancy Reynolds Re_b number. Gray marker filling indicates use of wall for top boundary condition. The final four cases reduce Re_b by changing the ambient density without stratification, i.e., $\rho_0 = \rho_B$.

2D/3D	S	Re_b	Top boundary	Symbol	Sections
2D	0.93	5000	Free-slip		F
2D	0.93	5000	Wall		F
2D	0.93	14 142	Free-slip		B D F
2D	0.93	14 142	Wall		D F
3D	0	14 142	Free-slip		A B C G
3D	0.2	14 142	Free-slip		A B C G
3D	0.4	14 142	Free-slip		A B C G
3D	0.93	14 142	Free-slip		A B C G
3D	0	14 142	Wall		B
3D	0.2	14 142	Wall		B
3D	0.4	14 142	Wall		B
3D	0.93	14 142	Wall		B
2D	0	6086	Free-slip		E
2D	0	10 741	Free-slip		E
2D	0	14 142	Free-slip		E
2D	0.8	14 142	Free-slip		E

precise; however, this would introduce a boundary layer at the rear of the current with demanding grid-point requirements with little expected effect on the current head dynamics which is being investigated here. Accordingly, the right-hand side of the tank boundary condition is unimportant until the current reaches one depth scale of the boundary.[10] The choice of spanwise periodicity neglects the boundary layer that would form near the tank side walls in the experiment and so our present findings are expected to be similar to the conditions into the tank mid-plane, away from the side walls.

The cases run in the present study are shown in Table III. The ambient fluid density at the top of the domain ρ_0 is held constant and the density at the bottom ρ_B is adjusted to obtain the required stratification intensity S. As per the definition of buoyancy velocity U_b, the buoyancy Reynolds number Re_b is thus constant for all cases. Furthermore, there are several objectives in this manuscript that each require separate combinations of the available data. Accordingly, Table III states which data are used for corresponding sections in the results in Sec. III. As a guiding principle, we regard the 3D free-slip simulations as the primary dataset for investigation in this manuscript, as we believe this is the most numerically accurate representation of the lock-exchange problem. Briefly, each section aims to address the following research objectives:

- A: Similarity solutions of the current early after release, using the primary dataset
- B: Front location comparison of free-slip and no-slip top boundary condition, and 2D/3D simulation
- C: Front velocity time series, using the primary dataset
- D: Comparison of free-slip and no-slip top boundary condition effect on structure of the subcritical propagating current head and internal waves

TABLE IV. Summary of the stratification parameters considered in the present study and characteristics of generated internal waves.

S	Nh_0	Nh_0/U_b	U_w/U_b	Classification
0	0	0	0	…
0.2	0.63	0.45	0.14	Supercritical
0.4	0.9	0.632	0.2	Supercritical
0.93	1.36	0.967	0.31	Subcritical

- E: Effect of the internal gravity wave on the propagation of a gravity current, as determined by reducing Re_b without stratification
- F: Influence of the top boundary condition on internal wave generation and propagation, investigated through 2D simulations at two values of Re_b
- G: Data-driven evaluation of similarity solutions in the inertial propagation regime, using the primary dataset.

Thus, this manuscript aims to answer fundamental questions about similarity solutions in planar gravity currents using the primary dataset, and also evaluates the robustness of these findings and appropriateness of simulations methodology through toggling whether the simulation is 2D/3D, varying the buoyancy Reynolds number Re_b, and toggling the top boundary condition. Further, a summary of the stratification intensities that feature in the primary dataset and the resultant internal wave characteristics are given in Table IV.

C. Pertinent parameters and mathematical models

An understanding of the motion of gravity currents is gained in this paper by appropriate scaling arguments as has previously been applied in unstratified ambient lock-exchange gravity currents.[9] The scaling of profiles to demonstrate self-similarity requires velocity, time and length scales arising from the present physical system and in this section, the pertinent parameters will be reviewed. We will classify the present flows by corresponding buoyancy Reynolds number which has been shown to classify turbulence in stratified flows[45] and is commonly employed as a dimensionless parameter for work carried out similar to present efforts.[2,46] In the reference laboratory experiments carried out,[2] the buoyancy Reynolds Re_b number obtained was approximately 20 000. For the simulations carried out in this study, most of the results presented feature $Re_b = 14\,142$ but comparison with the reference laboratory experiments is considered appropriate because as Re_b increases there is a weakening influence on gravity current dynamics.[47] Note, lock-exchange experiments in an unstratified ambient fluid[48] showed that at low Reynolds numbers, the current head mixing zone increased with increasing Reynolds number owing to transition from Holmboe waves to a Kelvin–Helmholtz instability. Furthermore, the Schmidt number fixed to unity in this study contrasts the value in the reference laboratory experiments which were conducted with saline, whereby $Sc \approx 700$.

The strength of the ambient stratification is quantified by the non-dimensional stratification intensity defined as

$$S = \frac{\rho_B - \rho_0}{\rho_C - \rho_0}. \tag{5}$$

When cases are presented as stratified, we will only consider cases where the ambient density increases linearly from ρ_0 at the free surface to ρ_B at the bottom of the tank. We will also assume stable stratification, i.e., $\rho_C > \rho_B > \rho_0$, so $0 \le S \le 1$. The initial value of the passive scalar is C_C for $x < l_0$ and C_0 for $x > l_0$, i.e., the passive scalar seeds the heavy fluid upon release.

The motion of the propagating gravity current vertically displaces fluid parcels causing them to oscillate. For the present simulations conducted with $S > 0$, the ambient stratification will give rise to internal gravity waves with given intrinsic Brunt–Väisälä frequency and propagation velocity of the generated linear mode-one long wave is

$$N = \sqrt{\frac{g}{h_0}\frac{\rho_B - \rho_0}{\rho_0}} \quad \text{and} \quad U_w = \frac{Nh_0}{\pi}.$$

We define the internal wave Froude number as the ratio of an advecting gravity current front, and the internal wave propagation,

$$Fr = \frac{U_{slump}}{Nh_0}. \tag{6}$$

When the $Fr > 1/\pi = 0.318$, the initial slumping velocity is greater than the internal mode-one long wave and this state is termed "supercritical," where the head of the current propagates initially with internal wave trailing behind.

The above-mentioned pertinent parameters are useful both for flow classification and as characteristic scales to form inputs of theoretical self-similar solutions to governing equations. Several mathematical models have been proposed for the motion and dynamics of the gravity current with varying grades of approximation. Two of the most widely used model classes will be here considered. The first being box-models, which are composed of the volume continuity requirement paired with dynamic modeling, such as an inertial-buoyancy balance. Additionally, the box-model assumes a horizontally uniform distribution of dense fluid and neglects the observed "head" of the propagating current and is a purely kinematic model that assumes mass conservation. The second being the more rigorous self-similar solutions to the shallow water equations.[17,49] It is important to note that both the box and shallow water models assume there is no mixing. Models for entrainment and mixing in the gravity current have been considered.[50] In this paper, we will be assessing the suitability of present DNS results with the self-similar profiles which predicate similarity solutions. The similarity variable is $y = x/x_F(t)$ where $x_F(t)$ is the front location of the gravity current and thus the length of the current, and this paper informs the correct shape of $H(y)$ to satisfy the similarity solution,

$$h(y,t) = \phi(t)H(y), \tag{7}$$

where $h(y, t)$ is the height profile of the current, decomposed into $\phi(t)$ which preserves continuity and $H(y)$ is the self-similar current height profile shape. The determined theoretical profiles for $\phi(t)$ and $H(y)$ are compared in Table V.

In order to compare the collected 2D and 3D data with mathematical models of self-similar gravity currents, it is first required to define a height for the gravity current for a density field with mixing occurring. In the analysis of conducted experiments[9] for $S = 0$, an "equivalent height" $\bar{h}_\rho(x,t)$ for the current was defined by using the density field,

TABLE V. Comparison of the similarity profiles featured in Eq. (7) that determine the height profile of the propagating gravity current. Note that V is the volume of the gravity current with assumed no mixing, K is a constant, where $K = K_1 V^{1/3}$; $K_1 = [\frac{27}{2}\frac{Fr^2}{6-Fr^2}]^{1/3}$. Furthermore, the current front location x_F is defined in the present manuscript when Eq. (9) reaches a small threshold value.

Model		
Box model[17]	$\phi(t) = \frac{V}{x_F} = \frac{h_0 l_0}{x_F}$	$H(y) = 1$
Shallow water[17]	$\phi(t) = \frac{4}{9}K^3\frac{1}{x_F}$	$H(y) = \frac{1}{Fr^2} + \frac{1}{4}(y^2 - 1)$

$$\frac{\bar{h}_\rho(x,t)}{h_0} = \frac{\int_0^{L_y}(\bar{\rho} - \rho_O)dy}{\int_0^{L_y}(\rho_C - \rho_O)dy}, \tag{8}$$

where $\bar{\rho}(x,y,t)$ is the averaged density field in the homogeneous spanwise direction. From our experiences in post-processing the present data, it is difficult to detect the front and height of the current using $\bar{h}_\rho(x,t)$ consistently across our cases as potential contamination occurs from spurious contributions of the stratified ambient fluid. Instead, for this study, we define equivalent height based on the distribution of the passive scalar C,

$$\frac{\bar{h}_C(x,t)}{h_0} = \frac{\int_0^{L_y}(\bar{C} - C_O)dy}{\int_0^{L_y}(C_C - C_O)dy}, \tag{9}$$

where $\bar{C}(x,y,t)$ is the spanwise averaged value of C. The equation above gives an indication of the height of the gravity current at each x location that would occur in the absence of mixing, i.e.,

$$C(y) = \begin{cases} C_C, & y \le \bar{h}_C, \\ C_0, & y > \bar{h}_C. \end{cases} \tag{10}$$

Initially, in the ambient fluid, $x > l_0$, $\bar{h}_C = 0$ and $\bar{h}_C/h_0 = 1$ for $x < l_0$. For all times in our simulations $0 \le \bar{h}_C/h_0 \le 1$. The front location, x_F, is defined as when $\bar{h}_C$ reaches a small threshold value. It must be noted that when $S = 0$, $\bar{h}_C = \bar{h}_\rho$.

III. RESULTS AND DISCUSSION

A. Similarity at early stage

At the early stage of evolution, immediately after release, the gravity currents exhibit some universal scaling properties that can be revealed by applying arguments found in scaling laws for extremely strong thermals.[51] At this early stage, the flow is mostly driven by gravity (buoyancy) with the "reduced" gravity acceleration $g'_B = g(\rho_C - \rho_B)/\rho_B$, and its velocity is still very small. Note that the different stratified cases have different values of g'_B.

The pressure gradient has not been established yet so $p \approx p_0 = \text{const}$. Under these conditions the equations of motion reduce to a simple form $d^2h/dt^2 = -g'_B$ (free falling), where h is the height of the current close to the origin. Straightforward integration leads to the scaling law,

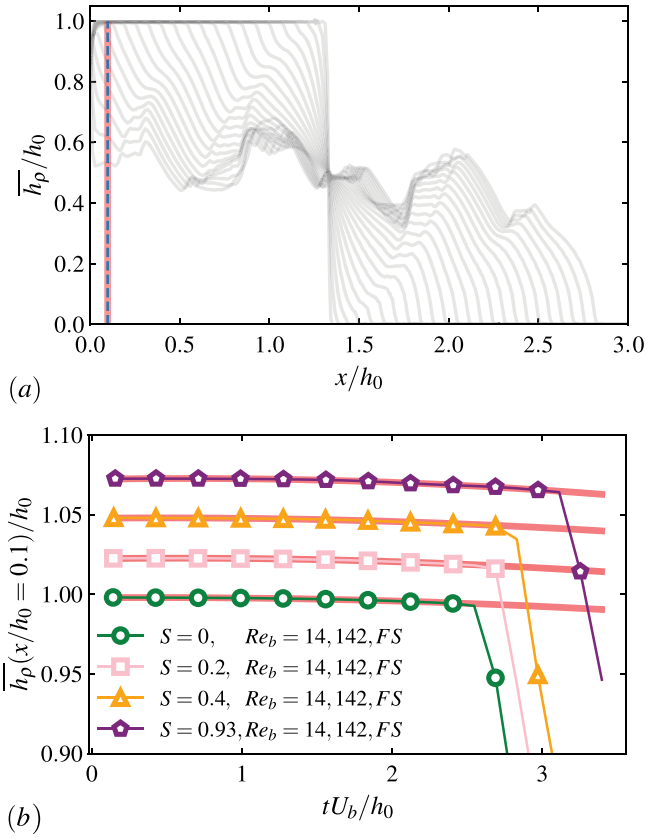

FIG. 3. (a) Equivalent height of the current at early times after release from the unstratified case ($S = 0$), from $tU_b/h_0 = [0, 3.5]$. Note the placement of probe at $x = 0.1$ denoted by the pink and dashed line, and (b) equivalent height at probe location $x = 0.1$ as a function of time with quadratic decay plotted as reference, profiles shifted vertically to facilitate easier visualization.

$$h = h_0 - g_B' t^2, \tag{11}$$

where we imposed $dh/dt(t = 0) = 0$. This scaling is valid for $t \ll \sqrt{h_0/g_B'}$. Hence, one would expect plotting the value of the current height at $x \approx 0$ will see a decrease in current height as a function of t^2. This is shown in Fig. 3(a), the evolution of the profiles of $\bar{h}_\rho(x, t)$ is shown for the reference unstratified case. We pick a point $x/h_0 = 0.1$ and plot the quantity $\bar{h}_\rho(0.1, t)$ in Fig. 3(b) for all S. The pink line is a line of t^2 and the data point from the simulations goes through this pink line for all cases. Note that the lines for different S have been shifted upward for clarity. This shows that this early time scaling holds even when stratification is present in the ambient.

B. Front location and comparison with experimental data

The normalized front location of the gravity current, x_F is shown in Fig. 4. As part of the present effort to accurately gauge the appropriateness of numerical setup against the plotted experimental data, outputs of simulations featuring both free-slip and wall for the top boundary conditions are compared and contrasted. For all values of S, there is good agreement with experimental data for $tU_b/h_0 < 30$.

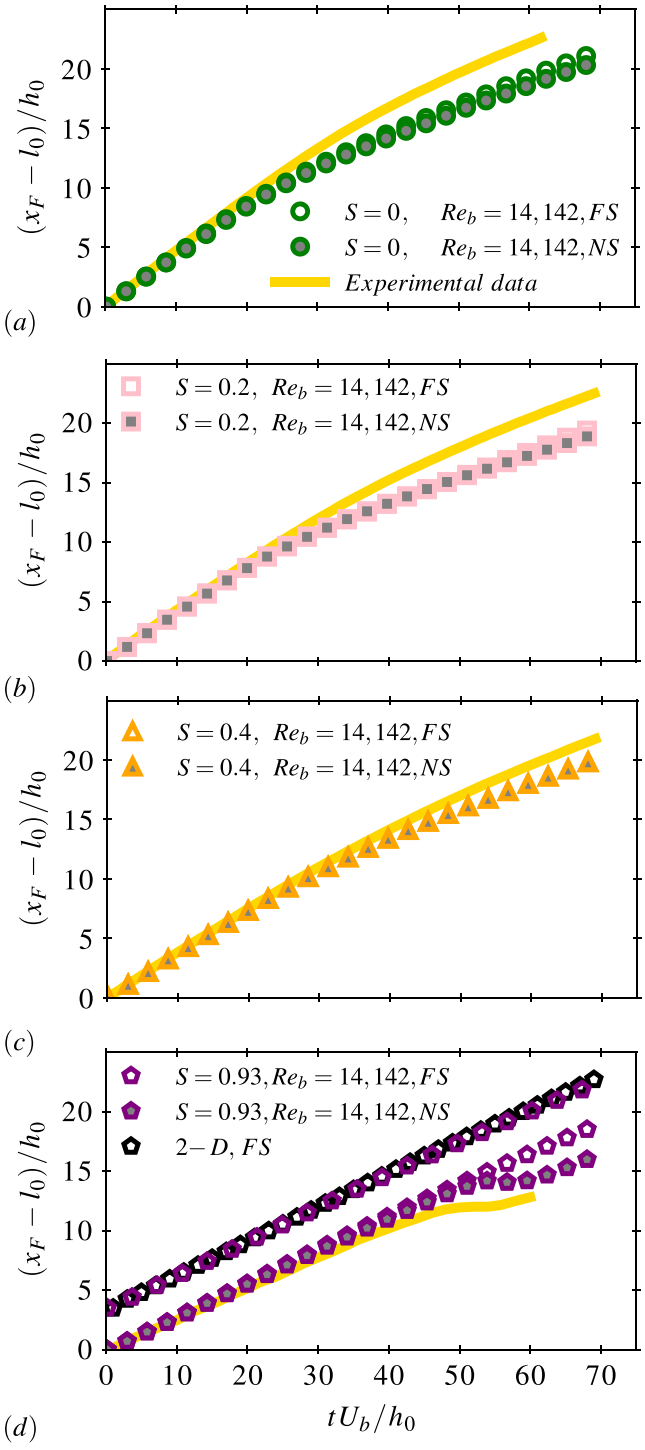

FIG. 4. Dimensionless front location of gravity current against dimensionless time for, (a) $S = 0$, (b) $S = 0.2$, (c) $S = 0.4$, and (d) $S = 0.93$ where the symmetric top boundary condition case is re-plotted along with 2D results with profiles shifted vertically. Markers correspond to present data with varying top boundary condition as denoted in Table III. Gold lines correspond to the experimental data obtained.[2]

In this interval, the propagation of the current front location appears linear, which is an observation that is corroborated by preceding partial- and full-depth lock-exchange laboratory experiments.[9] Beyond this time-interval, the agreement between present simulations and experiments for the $S = 0$ case suffers. However, qualitatively, both sets of data show a decelerating current. We report that relative to the experimental values, a defect emerges in the presented propagation of the current front location. For the unstratified case, the results of simulations with wall and free-slip top boundary conditions do not vary appreciably. The level of agreement between experimental and numerical data presented here is similar to previously reported findings in unstratified planar and cylindrical configurations of gravity currents.[12]

The agreement between experimental and present DNS data for time intervals beyond $tU_b/h_0 > 30$ is similar for the stratification intensity, $S = 0.2$ but for increased stratification, $S = 0.4$ the agreement improves and the experimental-to-DNS defect approximately halves. Furthermore, whether free-slip or wall is chosen as the top boundary condition for stratification intensities, $S = 0.2$ and $S = 0.4$, the resultant profile does not vary significantly.

However, this is no longer the case for high stratification $S = 0.93$. There are clear differences between the free-slip and wall top boundary numerical scenario for $S = 0.93$. This is the subcritical case ($Fr < 1/\pi$) where the internal gravity waves travel faster than the propagating gravity current. For the wall case, the front location decelerates at $tU_b/h_0 \approx 50$ but thereafter re-accelerates, which does not occur for the corresponding free-slip case in the restricted time-interval investigated in this section. Because the $S = 0.93$ case presents a departure from the agreement observed at lower stratification intensities between profiles generated with disparate top boundary conditions, closer attention is warranted. The difference between the wall and free-slip cases will be later explained by showing the evolution of isopycnals and contours of passive scalar C, and further analysis is presented in Secs. III D–III F. The present conclusion is that the subcritical $S = 0.93$ case reveals a pronounced influence of the top boundary condition choice. Furthermore, in Fig. 4(d), the corresponding 2D and 3D subcritical simulations with symmetric top boundary are offset for direct comparison, and it is established that front location profiles are well captured by 2D simulations, which has been reported previously.[2]

Figure 5 re-plots the data of the normalized front location of the gravity current, x_F data on a log–log scale to enable power-law fitting on a log–log graph (see, for example, application in power-law fluids,[52] or for gravity currents[11]). Additionally, only the present data generated with free-slip for top boundary condition are plotted. The different shades consist of data in the slumping, transition and inertia phases. The transition between phases of spreading lacks robust definition and precise onset times. To estimate the demarcated propagation phases, sophisticated approaches have been developed including matching front velocities from corresponding scaling laws[11] but presently we revert to a simple estimation of the onset of the inertial region. Here, we inspect the front velocity (shown in Sec. III C) and divide into constant-velocity, power-law decay velocity and the transition interval. We perform a least squares fit for data through each of these regions to a function of the form, $y = \alpha x^{\beta}$. The power law that we obtain is annotated in Fig. 5 and the function is graphed as a line.

It can be seen that in the slumping phase, the normalized front location x_F follows a $\sim t^1$ power law for all the ambient stratification

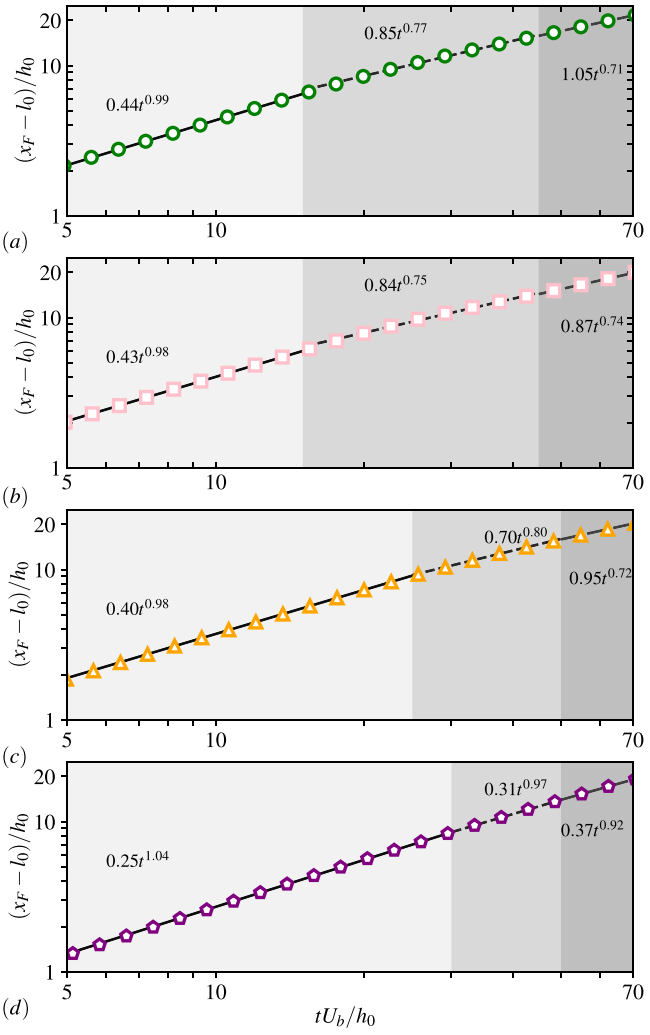

FIG. 5. Same as Fig. 4 but re-plotted on log–log scale. Markers correspond to data-generated in the present study and lines correspond to power-law fits in separate demarcated regions with power-law annotated.

considered, i.e., propagation of the front location is linear as in Fig. 4 and hence the propagation velocity is constant in this phase. However, the coefficient of this power law monotonically decreases with increasing stratification S from $\alpha = 0.44$ for the unstratified case to $\alpha = 0.25$ for $S = 0.93$. This indicates that the stratified environment decreases the front velocity during the slumping phase. The explanation for this trend is unsurprising and a consequence of our chosen constant dimensionless number, Re_b, which employs a buoyancy velocity U_b as the characteristic velocity scale. Framing the problem as constant Re_b ignores the variation in density at the bottom of the domain ρ_B, which is the parameter varied in this studied to achieve variation in stratification. For an increased stratification, there is an increased value of ρ_B and it follows a reduced density differential to drive the flow. With this in mind, our primary focus is the quantitative change of the exponent in the power law.

In the inertia phase, for the unstratified case, propagation of the current front x_F follows $\sim t^{0.71}$. The exponent of the power law does not change for $S = 0.2$ and 0.4 although for the latter case there is a slight delay in onset of the inertia regime and a longer transition region. However, it is clear that the exponent of the power law for the inertia phase for the $S = 0.93$ case is dramatically higher. For the subcritical flow environment, the trailing internal waves, which are traveling faster than (and therefore catching) the current-head, are also observed to partially drive the current.

C. Front velocity

The position of the front location identified by the passive scalar threshold yields a time-series which is differentiated to determine the front velocity, $u_F = dx_F/dt$. The normalized front velocity, u_F, plotted for the varying values of S, is shown in Fig. 6. The markers in the figure are directly down-sampled from the present DNS data. The plotted lines are computed by applying a Savitzky–Golay filter on the data to remove high frequency components that do not fall into our present attention, and the resulting smoothed lines form a visual guide to the data. It is apparent from the front velocity time-variation that several propagation phases exist and these have been extensively considered for unstratified planar- and cylindrical-release currents.[12]

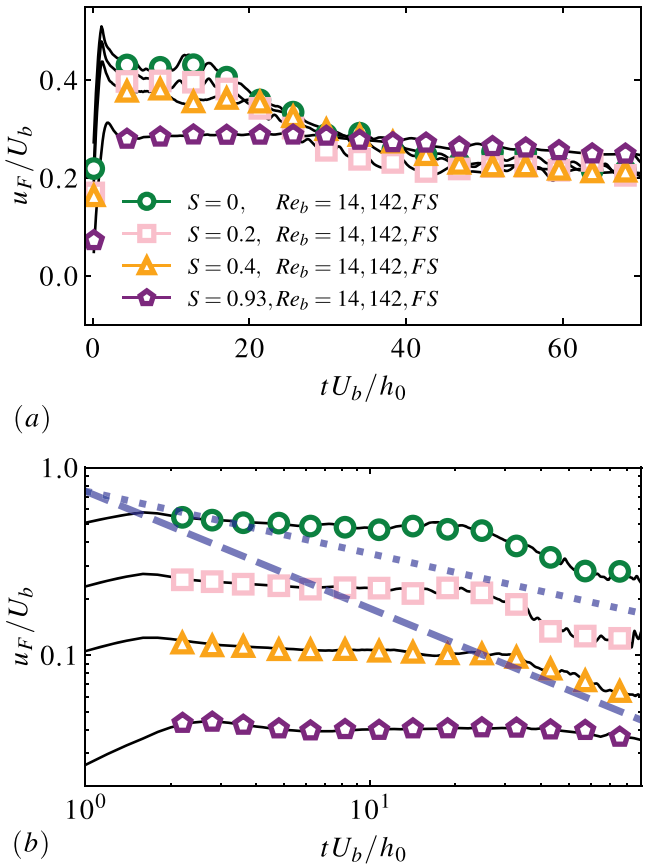

FIG. 6. (a) Front velocity of gravity current for the duration of the simulation, for ambient stratification strengths, $S = 0, 0.2, 0.4$, and 0.93 for the free-slip top boundary condition. The front velocity has been scaled by the buoyancy velocity, U_b, and (b) re-plotted on log–log scale where profiles are vertically shifted in order to assess the goodness of matching their slope to reference asymptotic behavior. Dotted line corresponds to $u_F/U_b \propto t^{-1/3}$ scaling and dashed to $u_F/U_b \propto t^{-5/8}$.

It is clear from Fig. 6(a) that initially all cases go through the acceleration phase and simultaneously reach a peak front velocity at $tU_b/h_0 \approx 2$. Thereafter, the front velocity rolls off to a near constant value in the slumping phase. The velocity of the slumping region is observed to decrease with increasing S. Furthermore, our data indicate that the gravity current exhibits a longer time interval in the slumping regime as stratification, S increases. After the slumping phase has completed, the front velocity for stratification intensities $S = 0, 0.2$, and 0.4 does not appreciably differ in the transition-inertia intervals. For the inertia phase, however, the front velocity for the subcritical $S = 0.93$ seems to be the highest, which indicates that it has not undergone the same velocity power law decay as the lower stratification cases.

Beyond the constant velocity slumping phase, the front velocity transitions to self-similar regimes where power-law expression are able to describe the front velocity decay. By balancing the buoyancy and inertial forces in a boundary layer approximation, for unstratified planar currents the front velocity decay has been established,[11]

$$u_F/U_b = \frac{2}{3}\xi_p (h_0 l_0)^{1/3} t^{-1/3}, \tag{12}$$

where ξ_p is a theoretical constant with various proposed values. Similarly by balancing in a boundary layer approximation, buoyancy, and viscous forces,[21]

$$u_F/U_b = \frac{3}{8}\xi_{pHt} h_0^{1/2} l_0^{1/2} Re_b^{1/8} t^{-5/8}, \tag{13}$$

where ξ_{pHt} is again a theoretical constant. Examining the validity of these scaling laws motivates re-plotting the front velocity onto a log–log plot in Fig. 6(b). The dimensionless front velocity u_F/U_b power law decay relations were derived for an unstratified ambient and therefore, their shift in time intervals of relevance when ambient stratification is incorporated remains unknown. Instead, much of the preceding analysis targeted toward gravity current front velocity has focused attention on higher Re where large undulations are the result of roll-up of the current due to Kelvin–Helmholtz instabilities.[12]

Since we are interested in incorporation of stratification, we remark in Fig. 6(b) that the unstratified $S = 0$ case is clearly suggestive of a power law decay and seems to match the predicted inertial decay, $u_F/U_b \propto t^{-1/3}$ at $tU_b/h_0 = 45$, and this onset time for inertial decay is the same for stratification intensity $S = 0.2$. For the $S = 0.4$ and $S = 0.93$ cases, we suggest a slight delay to onset of inertial decay, $tU_b/h_0 = 50$. This suggestion is quite pertinent for the $S = 0.4$ case but the existence of power law decay for stratification intensity $S = 0.93$ intensity is tenuous and conceptually retained here to facilitate comparisons of current propagation.

D. Density field isocontours: Structure of the subcritical propagating gravity current head and internal waves

It was noted in Sec. II C that propagation of the gravity current front in a stratified ambient fluid can be more clearly determined by contours of the passive scalar concentration, C, than the density field, ρ. However, when stratification of the ambient fluid is present, the

additional phenomena of internal waves occur in conjunction with the gravity current and detection of the internal waves is not possible through *C*. Consequently, we first turn attention to the connection between the generated internal waves and top boundary condition. This is investigated in the context of 2D simulations with $S = 0.93$.

Contours of the normalized density field $\rho^* = (\rho - \rho_0)/(\rho_C - \rho_0)$ are plotted for the case of the wall top boundary condition in Figs. 7(a)–7(f) and corresponding free-slip top boundary condition is shown in Figs. 7(g)–7(l). Isolines of lower ρ^* values are detected which reveal internal waves. In contrasting panels (a)–(c) and (g)–(i) in Fig. 7, it is readily apparent that there is little observable difference in the shape and size of the current head, the forming Kelvin–Helmholtz billows swept behind the front region, nor the internal waves. However, at $tU_b/h_0 = 30$, visualized in (j) of Fig. 7, the head begins splitting due to the presence a vortical motion for the symmetric top boundary condition case, but not when a wall is used as in Fig. 7(d). In the latter, an internal wave appears behind the gravity current front. The interaction of the gravity current and internal waves is informed by the current acceleration, which initially for a small interval travels at a speed that is faster than the wave.

The gravity current proceeds to decelerate to the slumping velocity and thereafter gradually decelerates. Eventually, the wave will "catch" the current; we will term this occurrence a "transition point." In Fig. 7(f), it is clear that the internal wave has suppressed the head of the gravity current in size and also cleaved the body of the current as intense ρ^* regions are visibly present at $x/h_0 = 12$ and 15. This is in contrast to the latter stage free-slip case, shown in Fig. 7(l), where big rolls feature throughout the current head. It remains to describe the dissimilarities in the structure of the isopycnals between the wall and free-slip cases. The internal wave wavelength appears longer in the free-slip case which is most evident in contrasting later time instances in Figs. 7(f) and 7(l), attributable to the longer current head present in the free-slip case. In the wall case, the shorter propagating current head has merged with the Kelvin–Helmholtz billows, whereas for the free-slip case, these billows seemed to continue to develop for the duration of visualized times.

An additional observation is that the generated internal wave has formed at a closer streamwise location for the wall case relative to the current front location. In the top left part of the numerical domain at early time instances, the isolines appear significantly more disordered which may indicate intense vorticity arising from the wall boundary condition. In order to corroborate this observation, we contrast the vorticity at an early time interval in Fig. 8 to see the effect of the top boundary condition on the formation of vortical structures. It is apparent that the vorticity associated with the current head is visually similar; however, it is clear that an intense vortical motion forms in the top left of the domain for the wall top boundary condition case. It is this structure that is responsible for the modified formation of the internal waves that will play a role in shifting the transition point of the internal wave interaction with the current head.

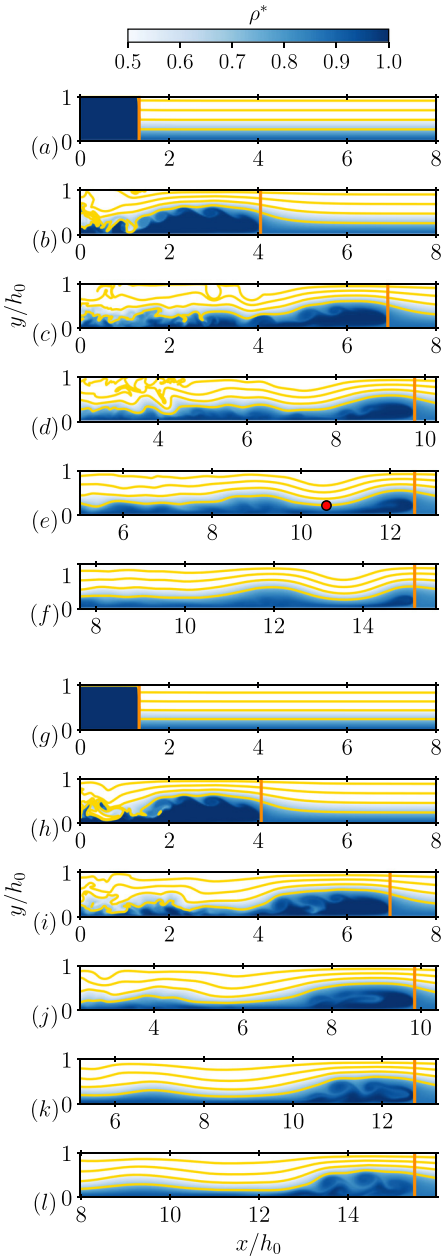

FIG. 7. Visualization of the 2D planar gravity current with wall as the top boundary on top, and free-slip on bottom. The gold isolines correspond to $\rho^* = 0.1$, 0.3, 0.5, 0.7. Times shown are (a) and (g) $tU_b/h_0 = 0$, (b) and (h) $tU_b/h_0 = 10$, (c) and (i) $tU_b/h_0 = 20$, (d) and (j) $tU_b/h_0 = 30$, (e) and (k) $tU_b/h_0 = 40$, and (f) and (l) $tU_b/h_0 = 50$. Vertical orange line denotes gravity current front. Note that in panel (e), the presence of a red-marker denotes the location of a local minima in the generated internal wave.

E. Effect of the internal gravity wave on the propagation of a gravity current

As mentioned in Sec. II A, the Reynolds number of the gravity current is calculated based on the density difference between the dense fluid and the ambient fluid at the top of the domain (ρ_0). However, in a stratified environment, a gravity current encounters varying degrees of density contrast between the heavier fluid and the surrounding ambient fluid at different wall-normal heights. For instance, the density difference between the heavy fluid and the ambient fluid at the top of the gravity current would be larger than at the bottom. Therefore,

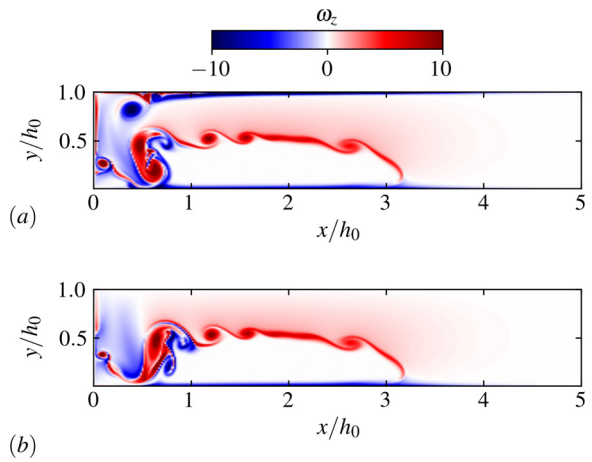

FIG. 8. Visualization of the vorticity ω_z, shown is the subcritical $S = 0.93$ case with $Re_b = 14\,142$ for the 2D planar gravity current at $tU_b/h_0 = 7$ for the top boundary condition set to (a) wall and (b) free-slip.

the local Reynolds number of the gravity current increases with wall-normal height. To separate the effects of Reynolds number from the influence of stratification (i.e., internal waves), the stratified gravity current with $S = 0.8$ at buoyancy Reynolds number of $Re_b = 14\,142$ is compared with unstratified gravity currents at $Re_b = 14\,142$, 10 741, and 6086 corresponding to the density difference at the top, mid-height and bottom of the stratified domain. It is postulated that the "effective" density difference of the gravity current with $S = 0.8$ is the density between the dense fluid and the mean density of the stratified ambient fluid, which is the density of the stratified ambient fluid at the domain mid-height.

Figure 9 illustrates the plot of the front location and front velocity of a planar gravity current propagating in different ambient conditions at $Re_b = 14\,142$, 10 741, and 6086. To compare the front location and velocity of the unstratified cases with the stratified cases, the velocity scale of the stratified gravity current is used to non-dimensionalize the front velocity and time.

It is evident that the unstratified ambient case with the highest Reynolds number coincides with the gravity current traveling further due to higher front velocity and conversely the lowest Re_b case travels slowest. The front location of the stratified case $S = 0.8$ is bounded by these two extremes. For the case with a moderate buoyancy Reynolds number $Re_b = 10\,741$, the front position of the current is similar to the stratified case $S = 0.8$ up to $tU_b/h_0 \approx 38$. Analyzing the front velocity of the gravity current for these two cases in Fig. 9(b), it is observed that they are in good agreement, especially in the constant velocity slumping phase $u_F/U_b \approx 0.32$ compared with $u_F/U_b \approx 0.31$ for the stratified $S = 0.8$ case. This indicates that stratification of the ambient fluid reduces the effective Reynolds number of the gravity current. Note that in Fig. 9(b) the gray horizontal solid line represents the velocity of the linear, mode-one, long internal gravity wave, Nh_0/π. The velocity of the stratified case $S = 0.8$ in the slumping phase is greater than this internal gravity wave, and therefore, the gravity current is in the super-critical regime.

Within the unstratified cases, the front velocity leaves the constant velocity phase at times $tU_b/h_0 \approx 16$, 25, and 33 for the high,

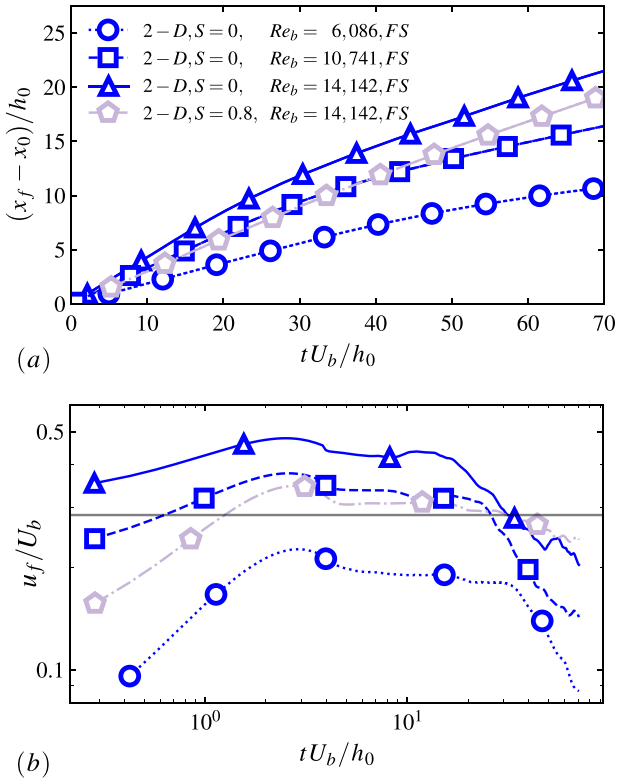

FIG. 9. Plot of the (a) front location and (b) front velocity as a function of time for gravity current propagating in the unstratified ambient at different buoyancy Reynolds numbers $Re_b = 14\,142$, 10 741, 6086 and the stratified case with $S = 0.8$ at $Re_b = 14\,142$. Additionally in (b), the velocity of the linear, mode-one, long wave NH/π is represented by a horizontal line.

moderate and low Re_b cases, respectively. Notably, the gravity current in the $S = 0.8$ case transitions into a subcritical flow ($Fr < 1/\pi$) at around $tU_b/h_0 \approx 30$, indicating the end of the slumping phase. Following the end of the slumping phase, the gravity current enters the self-similar regime. It is observed that the front velocity of the stratified case decays at a rate much smaller than the unstratified cases. This phenomenon is exclusively observed in the gravity current propagating in a linearly stratified ambient due to the influence of internal gravity waves. As the internal gravity wave generated at the lee side of the head of the gravity current propagates, it "pushes" the current and reduces the decay rate of the current's front velocity.

Figures 10 and 11 present the spanwise-averaged contours of the normalized passive scalar, illustrating the behavior of the unstratified cases at high, moderate, and low buoyancy Reynolds numbers, in conjunction with the stratified $S = 0.8$, $Re_b = 14\,142$ case. These visualizations are provided both at the slumping and self-similar phases at $tU_b/h_0 = 10$ and 50, respectively. Observation of Fig. 10 reveals that during the slumping phase, the gravity current flow becomes turbulent in all cases, leading to the generation of Kelvin–Helmholtz billows trailing behind the current. The position of the front of the stratified gravity current in Fig. 10(d) is comparable to the case at moderate Re_b in Fig. 10(b), albeit distinct differences in the structures behind the gravity current head are discernible.

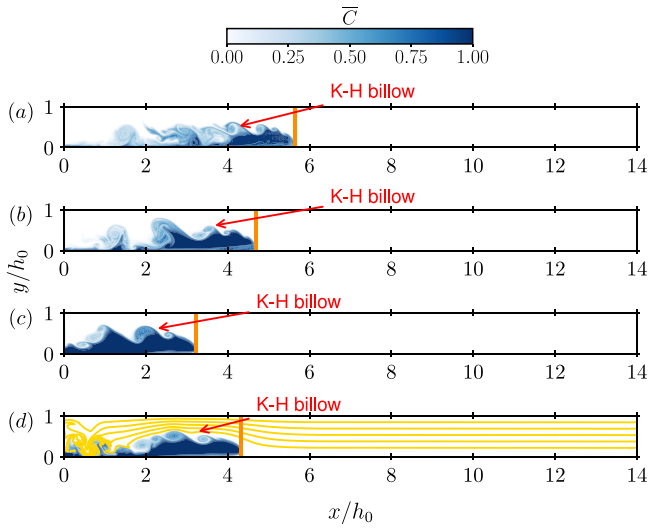

FIG. 10. Spanwise-averaged contour of the normalized passive scalar for the unstratified cases at different buoyancy Reynolds number Re_b = (a) 14 142, (b) 10 741, (c) 6086 and in, (d) $S = 0.8$ at $Re_b = 14\,142$. All contours are plotted for the gravity current in the slumping phase at $tU_b/h_0 = 10$ where the front velocity of the current is nearly constant. The solid gold lines in (d) represent the isopycnals. The orange vertical lines indicate the front position of the gravity current.

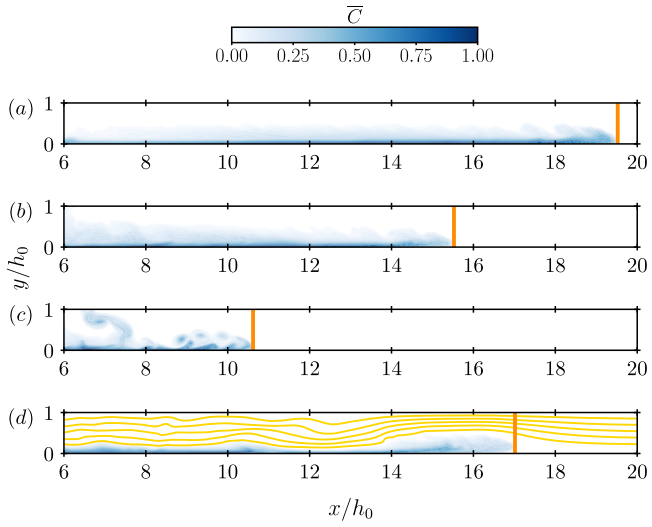

FIG. 11. Same as Fig. 10 at $tU_b/h_0 = 50$, which is now the self-similar inertia phase.

Notably, the size of the Kelvin–Helmholtz billows in the stratified case is considerably smaller and less turbulent. This phenomenon can be attributed to the influence of the ambient stratification inhibiting the motion of the Kelvin–Helmholtz billows, leading to more restrained and less turbulent behavior. At $tU_b/h_0 = 50$, the front of the stratified gravity current has traveled further than the unstratified case at moderate Re_b [see Figs. 11(b) and 11(d)] due to the slower velocity decay in the self-similar phase as presented previously in Fig. 9(b). The occurrence of internal waves can be observed in the contour lines of the isopycnals. The internal waves generated at the back of the head of the gravity current interact with the head of the gravity current and push it forward.

F. Influence of top boundary condition on internal wave generation and propagation

In Sec. III D, variation in the generated internal waves and current head morphology was documented for the higher stratification intensity $S = 0.93$. At subcritical Froude number Fr, the influence of the top boundary condition appears to be of greatest concern. Therefore, quantitative investigation of the effects of top boundary condition and buoyancy Reynolds number Re_b are crucial and in this section, it will be documented that results in the literature that obtain matched data between numerical results and laboratory experiments are merely fortunate.

To this end, the slumping velocity shown in Sec. III C is input to compute the Fr number and the ensuing relationship with stratification intensity S is plotted in Fig. 12(a). In general, the trend is for Froude number Fr to decrease as the ambient stratification gets larger, this is reflected by all data points in Fig. 12(a) and further, there is good agreement between the data reported here with the experimental reference data.[2,18] The data that features in this section is 2D and this is a safe numerical simplification given the comparison of 2D and 3D results earlier in the manuscript.

The initially trailing internal waves have an obviously important event of "transition" as they overrun the current head. It was shown in Fig. 7 for the wall top boundary condition case that current propagation decelerated once the internal waves caught up and suppressed the current head. It was also noted that the local minima of the trailing internal wave could be detected, and this was plotted in Fig. 7(e). The methodology to detect this local minima is prone to noise at early times, because the basic algorithm we have developed for this purpose simply filters the signal for regions where the spatial derivative flips from a threshold number of consecutive negative values to consecutive positive values.

Figure 12(b) shows the propagation of the normalized current front location for $S = 0.93$ both for buoyancy Reynolds number $Re_b = 5000$ and 14 142, as well as toggling free-slip and wall top boundary conditions. At early time instances, $tU_b/h_0 < 30$ all the determined profiles are in close agreement. Thereafter, the lower buoyancy Reynolds number $Re_b = 5000$ with wall top boundary condition undergoes transition first as evidenced by the current front deceleration/re-acceleration event pair, occurring at $tU_b/h_0 = 50$. The higher Reynolds number $Re_b = 14\,142$ case has a delayed onset of transition, occurring approximately at $tU_b/h_0 = 60$. Concerning the free-slip top boundary condition cases, there was no appreciable discrepancy after $tU_b/h_0 = 70$ time units and so the higher Reynolds number $Re_b = 14\,142$ case was run for a longer duration. After $tU_b/h_0 = 125$ time units, the same current front deceleration/re-acceleration event pair occurred as was present in the wall cases.

To complete the picture, in Fig. 12(c) we collate internal wave propagation as quantified by the detected trailing wave local minima for $Re_b = 14\,142$ to compare and contrast the boundary condition influence on propagation of the internal waves. For both cases, propagation of the internal wave is quite similar to the theoretical wave speed determined by the Brunt–Väisälä frequency after approximately

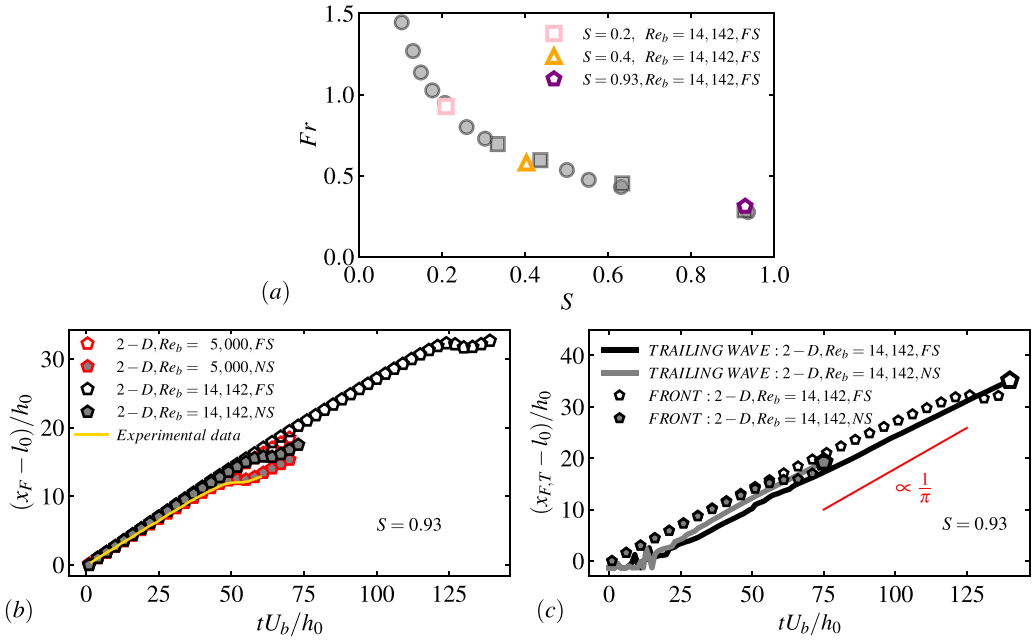

FIG. 12. (a) Plot of Froude number *Fr* in the slumping phase compared with experimental results of Dai *et al.*,[2] denoted by gray circles, and Maxworthy *et al.*,[18] denoted by gray squares. (b) Propagation for the subcritical $S = 0.93$ current front for $Re_b = 5000$ and 14 142, with wall and free-slip top boundary condition, in addition, gold line corresponds to experimental data,[2] and (c) solid lines for propagating trailing internal wave for $Re_b = 14\,142$ cases with contrasting top boundary conditions, and with diminished markers re-plotted for current front location. For clarity, at the end of the profile the corresponding case marker from Table III is plotted to facilitate ease of visual comparison. Also plotted in red is the propagation of trailing internal wave and theoretical propagation velocity of the generated linear mode-one long wave. All markers are consistent with those presented in Table III.

$tU_b/h_0 = 25$ time units. However, it is apparent that the internal wave forms slightly ahead for the wall top boundary condition, which causes an earlier cleaving of the current head. The transition point occurs at $tU_b/h_0 = 60$ for the wall case and $tU_b/h_0 = 125$ for the free-slip case. This coincides with the deceleration/re-acceleration event pair documented in Fig. 12(b). We postulate that the change in vorticity at the top boundary condition influences the formation of the internal wave.

Our contention is that for lock-exchange computational representation as presently considered, simplification of free surfaces via the rigid-lid approximation with free-slip boundary condition remains the most suitable choice. However, if agreement between the experimental results and numerical data is desired, tuning of the top boundary condition and Reynolds number may reliably achieve this aim.

The conclusion of this section provides an explanatory basis for the plethora of numerical modeling assumptions on simplifying representation of the top boundary condition and buoyancy Reynolds number Re_b that appear in reference literature.[2,15,18] In general, the transition phenomena inherent to subcritical gravity currents ($Fr < 1/\pi$) are not altered by the numerical assumptions investigated but corresponding the transition interval may be delayed. This finding is restricted to subcritical gravity currents because for supercritical gravity currents ($Fr > 1/\pi$) the current front and mode one long wave are locked together.[2]

G. Similarity solution

In this section, we will compare the present DNS-outputted scaled height profiles of the propagating current with predictions from the box model and similarity solutions of the shallow water equations, both detailed in Sec. II C. From the DNS data, we calculate equivalent height profiles h_C using only data in the inertia similarity phase. For $S = 0$, this corresponds to $tU_b/h_0 > 45$ as obtained from inspection of the front velocity in Fig. 6(b) and demarcated in Fig. 5. The gray lines in Fig. 13 show instantaneous realizations of the normalized values of h_C. The x axis is normalized by $x_F(t)$ and the y axis is normalized by $h_0 l_0 / x_F(t)$. The normalization is such that the area underneath all the curves integrates to unity in the absence of mixing. Accordingly, the time-average of all instantaneous solutions is also shown. The distribution of the heavy fluid appears to be self-similar for the unstratified propagating current in Fig. 13(a), at least naively insofar as the scaled instantaneous realizations are not significantly deviating from the time-averaged curve, i.e., the variance appears low and there is no time-dependent evolution of the scaled solution.

Evaluation via empirical data as to whether the shallow-water equation similarity solutions are appropriate representations of equivalent height profiles has been previously investigated[9] where it was determined qualitatively that the observed current had the same shape as the theoretical profiles and the increased fluid volume in the gravity current front was captured. For the unstratified case, the two most important deviations between the time-averaged scaled height of the gravity current when compared with the similarity solutions of the shallow-water equations are (i) the presence of additional oscillations in the current body which are of long wavelength approximately on the order of the current body and (ii) a slight overshoot in the height of the current head. Similar scaled profiles have been obtained in

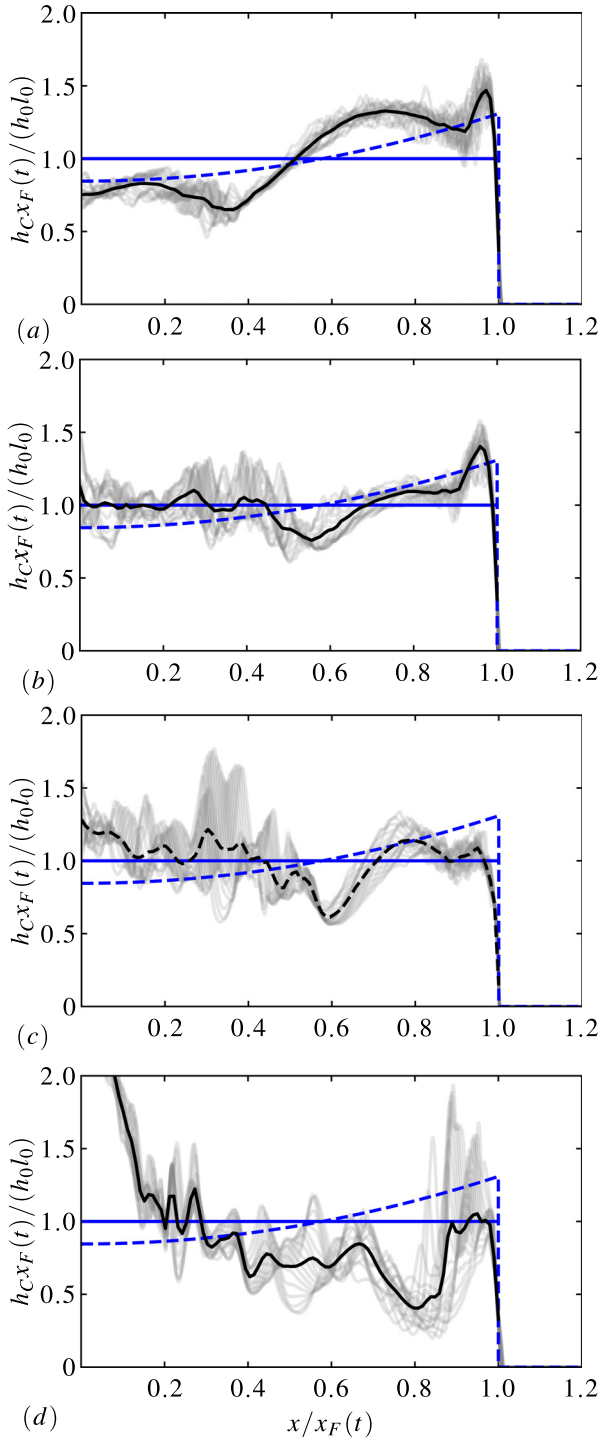

FIG. 13. Scaled equivalent height profiles $h_C(x,t)$ of the gravity current for 3D simulations with stratification (a) $S=0.0$, (b) $S=0.2$, (c) $S=0.4$, and (d) $S=0.93$, and $Re_b = 14\,142$. Gray lines are instantaneous realizations and black line corresponds to the time-averaged profile. Dashed blue line is the similarity solution to the shallow water equations with $Fr = 1.19$, and solid blue is the box model.

experiments of salt solutions[53] but there the scaled profiles did not have as clear prominence of additional oscillations in the current body. For the unstratified case shown in Fig. 13(a), the self-similar inertial phase does not appear adequately represented by the box model because the box model completely neglects inclusion of the observed oblique profile resulting from a coherent current head, more favorable agreement is obtained with the shallow water approach, and we ascertain self-similarity of the inertia phase through the collapsed profiles of the equivalent height h_c.

Moving to the case of weak stratification strength, $S=0.2$, equivalent height profiles are plotted in Fig. 13(b). Relative to the unstratified ambient profiles, there is a slight decrease in the fluid volume in the current head. In the current body, however, the profile appears flatter and does not follow the monotonically increasing profile from current rear-to-front suggested by the shallow water similarity solution. The essential difference between weakly stratified ambient and the unstratified case being the lack of internal waves in the latter suggests that for supercritical currents the presence of internal waves will act to inhibit heavy density fluid accumulating nearer to the current head. When the ambient stratification strength is increased to $S=0.4$ as shown in Fig. 13(c), there is no longer a discernible deeper current front, in this sense, it appears the box model is a better representation of the equivalent height profile than the shallow water model similarity solution. However, the profile remains oscillatory and the associated wavelength of the equivalent height profile appears much shorter than the oscillations present in the unstratified ambient cases. Finally, for the intensely stratified $S=0.93$ case, which is a subcritical propagating current, there is a departure from the phenomena described here for the unstratified and supercritical cases. For this case, there is a build-up of fluid in the rear of the current, shown through equivalent height profiles in Fig. 13(d). In contrast to the unstratified and supercritical Froude number Fr cases, for the $S=0.93$ case scaled equivalent height profiles, including the current body and head, there are evident complications toward formulation of a similarity solution introduced by the timescale associated with transition detailed in Sec. III F.

It is worth noting that some peculiar features of the front and head profile of the current (e.g., several decreasing bumps behind the front, see Fig. 13) can be interpreted with the conventional mathematical model of the nonlinear waves in a fluid. In this model, the front corresponds to a stepwise solution of a viscous flow in the two layer fluids of different density. The lower layer, in which the stepwise change occurs, corresponds to the gravity current, and all changes along the layer are assumed to be relatively small in comparison with the sharp step at the front and can be disregarded. Under these conditions, the evolution equation for the front reduces to the Korteweg–de Vries–Burgers (KdVB) equation,[54–58] which describes the interplay between nonlinear, viscous, and wave dispersion effects in the two-layer system. The properties and the solutions of the KdVB equation are well-known.[57,58] For instance, the stepwise solutions can be monotonic or oscillatory, with the oscillatory solutions having remarkably similar profiles to the ones depicted in Figs. 13(a) and 13(b). An important point is that the switch between two types of solutions is controlled by dissipation in the system[57,58] (i.e., the viscosity or Reynolds number Re_b in our case) and the strong dissipation can suppress these bumps completely (Ref. 57 argues that these bumps correspond to the solitons in the systems). These properties of the KdVB solutions are consistent with the results from our simulations. Further

verification of this assumption and estimation of the threshold value of Re_b that controls two regimes of front propagation (if it exists) is outside of the scope of the current study and will be reported in our future work.

Visually comparing the scaled profiles and gauging their similarity ideally requires enhancement through quantification and this will be achieved here through matrix factorization. First, we will construct a matrix, A, where each column vector will constitute a realization of the scaled profiles in Fig. 13. The A matrix has a singular value decomposition (SVD),[59]

$$A = U\Sigma V^T, \tag{14}$$

where the left and right singular vectors are denoted as U and V, respectively. The diagonal elements of Σ are the singular values which are arranged in order of magnitude, $\sigma_1 > \sigma_2 \ldots > \sigma_n$. The left columns of the left singular vector U are taken to be the modes of the scaled similarity profiles. More pertinently, the rows of V^T indicate times of relevance for the contribution of each mode.

In developing similarity solutions, we generally wish to first understand whether self-similar profiles exist. The singular values produced by the SVD are a natural first point to begin answering this question and are plotted in Fig. 14(a). Clearly, for all stratification intensities investigated, there is an order of magnitude more energy in the leading σ_0 mode but in the stratified $S = 0.93$ case there is significantly more energy in the σ_1 mode than for the unstratified case. Given the contributions the individual modes are linearly combined to reproduce the A matrix, we are able to analyze the relative contributions of the most energetic σ_0 mode in the proposed inertia similarity phase through the corresponding zeroth right singular vector V_0 which is shown in Fig. 14(b). Beginning with the unstratified case, the contribution of V_0 is steady across Δt^*, which is the time relative to the onset of the inertial self-similar regime. This is also the case for supercritical stratification intensities, $S = 0.2$ and 0.4. However, as was noted in Sec. III C, the existence of an inertial similarity phase as determined by matched front velocity decay with the theoretical decay is only purported to exist for the subcritical $Fr = 0.93$ case and congruently, the V_0 contribution shows a monotonic time dependency for this case, indicating that a similarity solution is not present. This illustrates the point that SVD has corroborated visual inspection of the scaled equivalent height profiles and cases where the most energized mode contribution is consistent in time indicates existence of a self-similar profile.

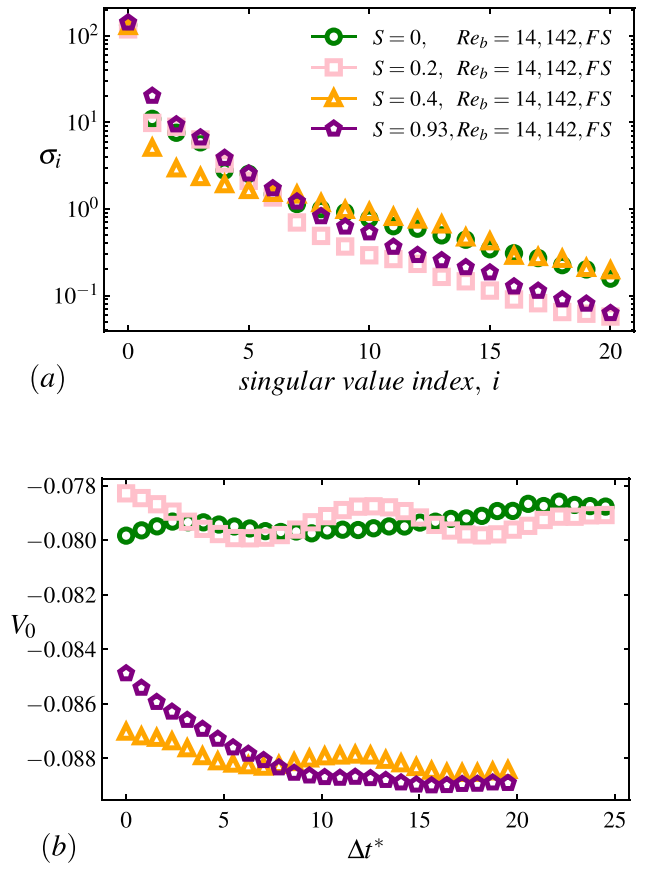

FIG. 14. Results of the singular value decomposition of the self-similar profile matrix, A: (a) the magnitude of the first 20 singular values, A, and (b) V_0, the leading right singular vector, during the proposed similarity phase. For this plot, Δt^* denotes time after the onset of the self-similar inertial regime in tU_b/h_0 time units.

H. Conclusion

The first principal novel contribution of the present work is a clearer understanding of the influence of the top boundary condition that approximates a free-surface in the lock-exchange gravity current context. Hitherto, it can be summarized that it had merely been documented that no-slip wall rather than more conventional rigid-lid boundary conditions in the simplified representation of a free surface may yield better agreement between numerical and laboratory experimental datasets, particularly as the stratification parameter S increases. It is documented here that choice of top boundary condition and specified Reynolds number can influence vorticity distributions in the domain and therefore modify the starting position of formed internal waves relative to the propagating current front. In a subcritical Fr number scenario, the consequence of an increased distance between internal waves and current front will be a delayed interaction between these two features. This results in a shift in the onset time of the momentary deceleration and re-acceleration event pair affecting the current front propagation. The findings here should clarify the limitations in simplified representations of free-surfaces and appropriate choice of top boundary condition where efficiency is required should be determined by the application being considered.

Concerning gravity current physics, the scaling of equivalent height profiles for propagating gravity currents in unstratified and linear inversely stratified ambient spanning sub- and supercritical Fr regimes has been investigated via DNS. The present contribution extends the established literature of asymptotic self-similar propagation phases originating from an instantaneous release by assessing whether such an approach remains valid when the ambient fluid is stratified. Additionally, a matrix composed of column vectors for instantaneous scaled height profiles restricted to the similarity phase is constructed. Subsequently, the SVD is computed furnishing a data-driven counterpart that quantitatively supplements the analysis. It was found that for lower values of S, where the corresponding Froude number Fr was subcritical, scaled profiles remained self-similar in the inertial phase, particularly closer to the current head. However, for the subcritical case with increased stratification $S = 0.93$, there appeared to

be a time-dependency on the resulting profiles. This finding was corroborated by the SVD analysis, which suggested a time-dependency of the leading mode contribution for the subcritical case. While the contributions of this paper have shed light on the geometrical self-similarity of gravity currents propagating into a stratified ambient, further questions have arisen about the capability of data-driven decomposition to identify potential for similarity solutions to governing equations which will form the basis of future work. Also, forming a focus for future work will be a comparative analysis between stratified and unstratified gravity currents to ascertain impact of ambient stratification strength on the small-scale mixing behavior through energy frameworks.[60]

ACKNOWLEDGMENTS

This research was fully supported by the Australian Government through the Australian Research Council's Discovery Projects funding scheme (Project No. DP210101965). Further, this work was supported by the computational resources provided by the Australian Government through NCI, Australia, under the National Computational Merit Allocation Scheme, the Pawsey's Energy and Resources Merit Allocation Scheme, and also the LIEF HPC-GPGPU Facility hosted at the University of Melbourne. This Facility was established with the assistance of LIEF Grant No. LE170100200.

AUTHOR DECLARATIONS

Conflict of Interest

The authors have no conflicts to disclose.

Author Contributions

Tony Zahtila: Conceptualization (equal); Data curation (equal); Investigation (equal); Methodology (equal); Software (equal); Visualization (equal). **Wai Kit Lam:** Conceptualization (equal); Data curation (equal); Visualization (equal). **Leon Chan:** Conceptualization (equal); Investigation (equal); Validation (equal). **Duncan Sutherland:** Conceptualization (equal); Formal analysis (equal); Methodology (equal). **Khalid Moinuddin:** Conceptualization (equal); Methodology (equal); Supervision (equal). **Albert Dai:** Conceptualization (equal); Methodology (equal); Supervision (equal). **Alexei Skvortsov:** Conceptualization (equal); Formal analysis (equal); Supervision (equal). **Richard Manasseh:** Conceptualization (equal); Methodology (equal); Supervision (equal). **Andrew Ooi:** Conceptualization (equal); Formal analysis (equal); Software (equal); Supervision (equal); Validation (equal).

DATA AVAILABILITY

The data that support the findings of this study are available from the corresponding author upon reasonable request.

REFERENCES

[1]H. E. Huppert, "Gravity currents: A personal perspective," J. Fluid Mech. **554**, 299–322 (2006).
[2]A. Dai, Y.-L. Huang, and Y.-M. Hsieh, "Gravity currents propagating at the base of a linearly stratified ambient," Phys. Fluids **33**, 066601 (2021).
[3]J. B. Simmons, C. Paton-Walsh, A. P. Mouat, J. Kaiser, R. S. Humphries, M. Keywood, D. W. T. Griffith, A. Sutresna, T. Naylor, and J. Ramirez-Gamboa, "Bushfire smoke plume composition and toxicological assessment from the 2019–2020 Australian black summer," Air Qual., Atmos. Health **15**, 2067–2089 (2022).
[4]N. P. Lareau and C. B. Clements, "Cold smoke: Smoke-induced density currents cause unexpected smoke transport near large wildfires," Atmos. Chem. Phys. **15**, 11513–11520 (2015).
[5]H. Huppert and J. Simpson, "The slumping of gravity currents," J. Fluid Mech. **99**, 785–799 (1980).
[6]J. W. Rottman and J. E. Simpson, "Gravity currents produced by instantaneous releases of a heavy fluid in a rectangular channel," J. Fluid Mech. **135**, 95–110 (1983).
[7]J. Hacker, P. F. Linden, and S. B. Dalziel, "Mixing in lock-release gravity currents," Dyn. Atmos. Oceans **24**, 183–195 (1996).
[8]J. O. Shin, S. B. Dalziel, and P. F. Linden, "Gravity currents produced by lock exchange," J. Fluid Mech. **521**, 1–34 (2004).
[9]B. M. Marino, L. P. Thomas, and P. F. Linden, "The front condition for gravity currents," J. Fluid Mech. **536**, 49–78 (2005).
[10]C. Härtel, E. Meiburg, and F. Necker, "Analysis and direct numerical simulation of the flow at a gravity-current head. Part 1. Flow topology and front speed for slip and no-slip boundaries," J. Fluid Mech. **418**, 189–212 (2000).
[11]M. I. Cantero, S. Balachandar, M. H. García, and J. P. Ferry, "Direct numerical simulations of planar and cylindrical density currents," J. Appl. Mech. **73**, 923 (2006).
[12]M. I. Cantero, J. R. Lee, S. Balachandar, and M. H. Garcia, "On the front velocity of gravity currents," J. Fluid Mech. **586**, 1–39 (2007).
[13]S. K. Ooi, G. Constantinescu, and L. Weber, "Numerical simulations of lock-exchange compositional gravity current," J. Fluid Mech. **635**, 361–388 (2009).
[14]J. E. Simpson, *Gravity Currents: In the Environment and the Laboratory* (Cambridge University Press, 1999).
[15]J. Pelmard, S. Norris, and H. Friedrich, "LES grid resolution requirements for the modelling of gravity currents," Comput. Fluids **174**, 256–270 (2018).
[16]W. K. Lam, L. Chan, D. Sutherland, R. Manasseh, K. Moinuddin, and A. Ooi, "Effect of stratification on the propagation of a cylindrical gravity current," J. Fluid Mech. (to be published).
[17]M. Ungarish, *An Introduction to Gravity Currents and Intrusions* (Chapman and Hall/CRC, 2009).
[18]T. Maxworthy, J. Leilich, J. E. Simpson, and E. H. Meiburg, "The propagation of a gravity current into a linearly stratified fluid," J. Fluid Mech. **453**, 371–394 (2002).
[19]V. K. Birman, E. Meiburg, and M. Ungarish, "On gravity currents in stratified ambients," Phys. Fluids **19**, 86602–86610 (2007).
[20]J. Zhou and S. K. Venayagamoorthy, "Impact of ambient stable stratification on gravity currents propagating over a submerged canopy," J. Fluid Mech. **898**, A15 (2020).
[21]D. P. Hoult, "Oil spreading on the sea," Annu. Rev. Fluid Mech. **4**, 341–368 (1972).
[22]J. E. Simpson, "Gravity currents in the laboratory, atmosphere, and ocean," Annu. Rev. Fluid Mech. **14**, 213–234 (1982).
[23]G. I. Barenblatt, *Scaling, Self-Similarity, and Intermediate Asymptotics: Dimensional Analysis and Intermediate Asymptotics* (Cambridge University Press, 1996), Vol. 14.
[24]A. J. Hogg, M. Ungarish, and H. E. Huppert, "Particle-driven gravity currents: Asymptotic and box model solutions," Eur. J. Mech.-B **19**, 139–165 (2000).
[25]A. C. Slim and H. E. Huppert, "Self-similar solutions of the axisymmetric shallow-water equations governing converging inviscid gravity currents," J. Fluid Mech. **506**, 331–355 (2004).
[26]Y. Cao, J. Philip, and A. Ooi, "Characteristics of a buoyant plume in a channel with cross-flow," Int. J. Heat Fluid Flow **93**, 108899 (2022).
[27]T. Bonometti and S. Balachandar, "Effect of Schmidt number on the structure and propagation of density currents," Theor. Comput. Fluid Dyn. **22**, 341–361 (2008).
[28]J. W. L. Paul, F. Fischer, and S. G. Kerkemeier, see http://nek5000.mcs.anl.gov for "nek5000 Web page" (2008).
[29]L. Lafayette, G. Sauter, L. Vu, and B. Meade, "Spartan performance and flexibility: An HPC-cloud chimera," in OpenStack Summit, Barcelona, 2016.

[30]W. Lu, D. Aljubaili, T. Zahtila, L. Chan, and A. Ooi, "Asymmetric wakes in flows past circular cylinders confined in channels," J. Fluid Mech. **958**, A8 (2023).
[31]A. Noorani, G. El Khoury, and P. Schlatter, "Evolution of turbulence characteristics from straight to curved pipes," Int. J. Heat Fluid Flow **41**, 16–26 (2013).
[32]W. Lu, Q. D. Nguyen, L. Chan, C. Lei, and A. Ooi, "Flows past cylinders confined within ducts. Effects of the duct width," Int. J. Heat Fluid Flow **104**, 109208 (2023).
[33]T. Zahtila, L. Chan, A. Ooi, K. Liu, M. Benjamin, and G. Iaccarino, "Influence of Miura-origami shapes on drag in turbulent flows," in *Proceedings of the Summer Program 2022*, Annual Research Briefs (Center for Turbulence Research, Stanford University, 2022).
[34]T. Zahtila, W. Lu, L. Chan, and A. Ooi, "A systematic study of the grid requirements for a spectral element method solver," Comput. Fluids **251**, 105745 (2023).
[35]A. Dai, "High-resolution simulations of downslope gravity currents in the acceleration phase," Phys. Fluids **27**, 076602 (2015).
[36]V. Birman, J. Martin, and E. Meiburg, "The non-Boussinesq lock-exchange problem. Part 2. High-resolution simulations," J. Fluid Mech. **537**, 125–144 (2005).
[37]A. Adcroft, C. Hill, J.-M. Campin, J. Marshall, and P. Heimbach, "Overview of the formulation and numerics of the MIT GCM," in Proceedings of the ECMWF Seminar Series on Numerical Methods, Recent Developments in Numerical Methods for Atmosphere and Ocean Modelling (2004) pp. 139–149.
[38]A. Kidanemariam and I. Marusic, "On the turbulence-generated free-surface waves in open-channel flows," in Proceedings of the 22nd Australasian Fluid Mechanics Conference (AFMC2020), 2020.
[39]S. Kara, M. C. Kara, T. Stoesser, and T. W. Sturm, "Free-surface versus rigid-lid LES computations for bridge-abutment flow," J. Hydraul. Eng. **141**, 04015019 (2015).
[40]M. A. Khodkar, K. El Allam, and E. Meiburg, "Intrusions propagating into linearly stratified ambients," J. Fluid Mech. **844**, 956–969 (2018).
[41]L. Ottolenghi, C. Adduce, R. Inghilesi, V. Armenio, and F. Roman, "Entrainment and mixing in unsteady gravity currents," J. Hydraul. Res. **54**, 541–557 (2016).
[42]X. Liu and Y. Jiang, "Direct numerical simulations of boundary condition effects on the propagation of density current in wall-bounded and open channels," Environ. Fluid Mech. **14**, 387–407 (2014).
[43]A. R. Horner-Devine and C. C. Chickadel, "Lobe-cleft instability in the buoyant gravity current generated by estuarine outflow," Geophys. Res. Lett. **44**, 5001–5007, https://doi.org/10.1002/2017GL072997 (2017).
[44]T. Agrawal, S. H. Peddada, and V. K. Chalamalla, "Dynamics of a buoyant gravity current propagating in a linearly stratified medium," Phys. Fluids **34**, 076605 (2022).
[45]W. D. Smyth and J. N. Moum, "Length scales of turbulence in stably stratified mixing layers," Phys. Fluids **12**, 1327–1342 (2000).
[46]J. Pelmard, S. Norris, and H. Friedrich, "Statistical characterisation of turbulence for an unsteady gravity current," J. Fluid Mech. **901**, A7 (2020).
[47]A. Dai and Y-l Huang, "High-resolution simulations of non-Boussinesq downslope gravity currents in the acceleration phase," Phys. Fluids **28**, 026602 (2016).
[48]P. Mukherjee and S. Balasubramanian, "Energetics and mixing efficiency of lock-exchange gravity currents using simultaneous velocity and density fields," Phys. Rev. Fluids **5**, 063802 (2020).
[49]R. T. Bonnecaze, H. E. Huppert, and J. R. Lister, "Particle-driven gravity currents," J. Fluid Mech. **250**, 339–369 (1993).
[50]M. A. Hallworth, H. E. Huppert, and J. C. Phillips, "Entrainment into two-dimensional and axisymmetric turbulent gravity currents," J. Fluid Mech. **308**, 289 (1996).
[51]A. Skvortsov, T. C. DuBois, M. Jamriska, and M. Kocan, "Scaling laws for extremely strong thermals," Phys. Rev. Fluids **6**, 053501 (2021).
[52]R. Sayag and M. G. Worster, "Axisymmetric gravity currents of power-law fluids over a rigid horizontal surface," J. Fluid Mech. **716**, R5 (2013).
[53]D. Sher and A. W. Woods, "Gravity currents: Entrainment, stratification and self-similarity," J. Fluid Mech. **784**, 130–162 (2015).
[54]D. H. Peregrine, "Calculations of the development of an undular bore," J. Fluid Mech. **25**, 321–330 (1966).
[55]R. S. Johnson, "A non-linear equation incorporating damping and dispersion," J. Fluid Mech. **42**, 49–60 (1970).
[56]R. S. Johnson, "Shallow water waves on a viscous fluid-the undular bore," Phys. Fluids **15**, 1693–1699 (1972).
[57]L. A. Ostrovsky and A. I. Potapov, *Modulated Waves: Theory and Applications* (Johns Hopkins University Press, Baltimore/London, 1999).
[58]G. B. Whitham, *Linear and Nonlinear Waves* (John Wiley and Sons, 1999).
[59]S. M. Hirsh, B. W. Brunton, and J. N. Kutz, "Data-driven spatiotemporal modal decomposition for time frequency analysis," Appl. Comput. Harmon. Anal. **49**, 771–790 (2020).
[60]W. K. Lam, L. Chan, Y. Cao, D. Sutherland, R. Manasseh, K. Moinuddin, and A. Ooi, "Mixing of a cylindrical gravity current in a stratified ambient," Int. J. Heat Fluid Flow (submitted 2024).